Lawrence Berkeley National Laboratory

Title
Spatial and temporal uplift history of South America from calibrated drainage analysis

Authors
Tribaldos, V Rodríguez
White, NJ
Roberts, GG
et al.

Spatial and temporal uplift history of South America from calibrated drainage analysis

V. Rodríguez Tribaldos

N. J. White

G. G. Roberts

M. J. Hoggard

Abstract

A multidisciplinary approach is used to analyze the Cenozoic uplift history of South America. Residual depth anomalies of oceanic crust abutting this continent help to determine the pattern of present-day dynamic topography. Admittance analysis and crustal thickness measurements indicate that the elastic thickness of the Borborema and Altiplano regions is ≤ 10 km with evidence for sub-plate support at longer wavelengths. A drainage inventory of 1827 river profiles is assembled and used to investigate landscape development. Linear inverse modeling enables river profiles to be fitted as a function of the spatial and temporal history of regional uplift. Erosional parameters are calibrated using observations from the Borborema Plateau and tested against continent-wide stratigraphic and thermochronologic constraints. Our results predict that two phases of regional uplift of the Altiplano plateau occurred in Neogene times. Regional uplift of the southern Patagonian Andes also appears to have occurred in Early Miocene times. The consistency between observed and predicted histories for the Borborema, Altiplano, and Patagonian plateaux implies that drainage networks record coherent signals that are amenable to simple modeling strategies. Finally, the predicted pattern of incision across the Amazon catchment constrains solid sedimentary flux at the Foz do Amazonas. Observed and calculated flux estimates match, suggesting that erosion and deposition were triggered by regional Andean uplift during Miocene times.

1 Introduction

The asymmetric physiography of South America can be divided into three parts: first, a young, subduction-related Andean chain that runs along its western margin; second, the central low plains of the Amazon Basin; and third, landforms of the Guyana, Brazilian, and Atlantic shields that are regarded as remnants of Late Precambrian and Early Phanerozoic orogenies [e.g *Almeida et al.*, 2000; *Ramos,* 2009]. Development of the South American landscape is driven by some combination of crustal and sublithospheric processes that interact to sculpt the

present-day surface [e.g., *Isaks*, [1988](#); *Lamb and Hoke*, [1997](#); *Almeida et al.*, [2000](#); *Hackspacher and Ribeiro*, [2004](#); *Blisniuk et al.*, [2005a](#); *McQuarrie et al.*, [2008a](#); *Barnes and Ehlers*, [2009](#); *Morais Neto et al.*, [2009](#); *Thomson et al.*, [2010](#)]. Regional topography is characterized by a series of long-wavelength swells. Examples include the Borborema Plateau of northeast Brazil, the Altiplano of the Central Andes, and plateaux of the Patagonian Andes. At these long wavelengths, convective circulation of the mantle probably plays some role in modifying regional topography, since crustal thickness measurements combined with isostatic considerations suggest that some component of long-wavelength topography is supported by sub-plate processes [*Haschke et al.*, [2006](#); *Assumpção et al.*, [2013](#); *Rossetti et al.*, [2013](#); *Yarce et al.*, [2014](#); *Almeida et al.*, [2015](#)].

Numerous studies focus on the dynamic topographic consequences of flat slab subduction and slab windows along the western margin of the continent [*Guillaume et al.*, [2009, 2013](#); *Dávila et al.*, [2010](#); *Dávila and Lithgow-Bertelloni*, [2013](#); *Eakin et al.*, [2014](#); *Dávila and Lithgow-Bertelloni*, [2015](#)]. There is also considerable interest in constraining uplift rates, especially within the Andean Cordillera [e.g., *Gregory-Wodzicki*, [2000](#); *Thomson et al.*, [2001](#); *Blisniuk et al.*, [2005a](#); *Ghosh et al.*, [2006a](#); *Horton et al.*, [2010](#); *Garzione et al.*, [2014](#)] and along the Atlantic margin [e.g., *Harman et al.*, [1998](#); *Cogné et al.*, [2012](#); *Japsen et al.*, [2012](#); *Jelinek et al.*, [2014](#)]. A key focus is the generation of well-resolved spot measurements, which inevitably have limited spatial coverage. Here, we are interested in exploring how spatial and temporal analyses of ubiquitous drainage networks can be exploited, subject to careful independent calibration, to extract continent-wide uplift rates. We apply the linearized methodology described by *Rudge et al.* [[2015](#)]. This efficient method enables simultaneous inverse modeling of substantial inventories of longitudinal river profiles as a function of regional uplift. Our goal is to identify coherent spatial and temporal patterns of regional uplift that illuminate our understanding of dynamic processes which contribute to the Cenozoic topographic architecture of South America.

2 General Framework

South American topography is dominated by the Andean chain, extending more than 8000 km along its Pacific margin (Figures [1](#)a and [1](#)b) [*Ramos*, [2009](#)]. This chain has a mean elevation of 4 km with several peaks exceeding 5 km and is characterized by elevated plateaux. The Central Andean Altiplano has a mean elevation of about 4 km and is the second highest plateau on Earth. Low relief plateaux are common as far south as Patagonia. East of the Andes Mountains, expansive lowlands of the Amazon and Paraná drainage basins dominate the landscape. To the north and east, these lowlands are interrupted by elevated plateaux of the Guyanan, Brazilian,

and Atlantic Shields. Large earthquakes are focused along the active margin, although intraplate seismicity occurs throughout the continent [*Assumpção et al.*, 2004, 2013; *Bezerra et al.*, 2006; *Bilek*, 2010].
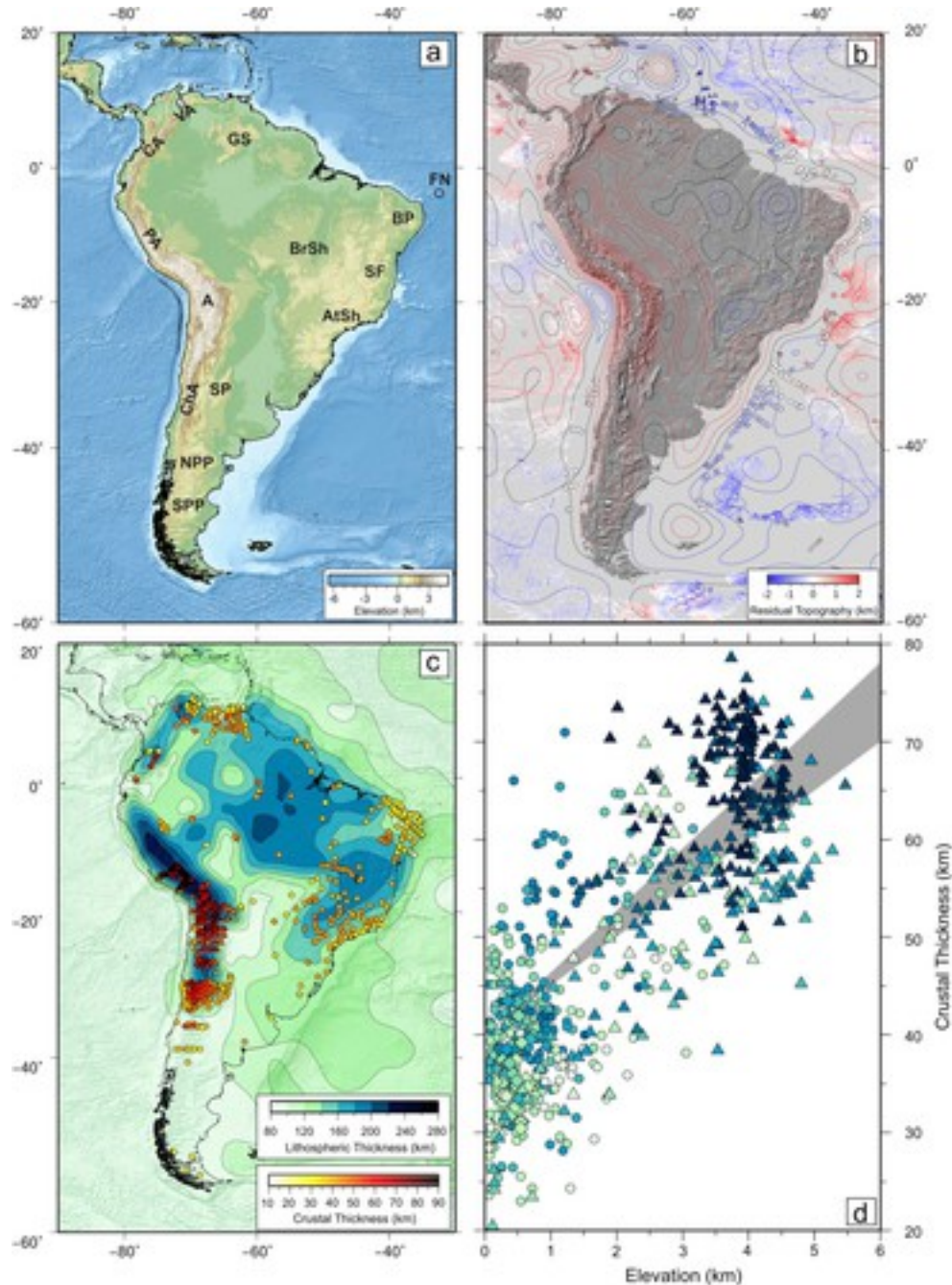

Figure 1
Open in figure viewerPowerPoint

(a) Topographic map of South America. VA = Venezuelan Andes; CA = Colombian Andes; PA = Peruvian Andes; A = Central Andean Altiplano; ChA = Chilean Andes; SP = Sierras Pampeanas; NPP = Northern Patagonian Plateau; SPP = Southern Patagonian Plateau; GS = Guyana Shield;

BP = Borborema Province; BrSh = Brazilian Shield; SF = São Francisco craton; AtSh = Atlantic Shield; FN = Fernando de Noronha. (b) Map of oceanic residual depth anomalies measured from seismic reflection and wide-angle surveys [*Hoggard et al.*, 2017]. Colored circles and upward/downward triangles = accurate estimates and lower/upper bounds; filigree of lines = less accurate estimates calculated from ship-track bathymetry. Red/black/blue contours = positive/zero/negative long-wavelength (i.e., > 730 km) non-hydrostatic gravity anomalies at 10 mGal intervals [*Mayer-Guerr*, 2015]. (c) Map of lithosphere thickness with contour interval of 20 km calculated from surface wave tomography [*Priestley and McKenzie*, 2013]. Colored circles = crustal thickness measurements from seismic wide-angle experiments, receiver function analyses and surface-wave dispersion studies [from compilation of *Assumpção et al.*, 2013]; triangles = measurements from Central Andean Altiplano; diamonds = measurements from Borborema Province. (d) Crustal thickness plotted as function of elevation where color indicates lithospheric thickness taken from (c). Gray band = expected isostatic relationship between crustal thickness and elevation for 30 km thick crust (width of band = range of crustal densities (i.e., 2.8 $\pm$ 0.05 Mg m^{-3}) for lithospheric mantle density of 3.3 Mg m^{-3}).

[Caption](#)

Crustal thickness measurements compiled from seismic wide-angle experiments, from receiver function analysis, and from surface-wave dispersion studies reveal significant continent-wide variations (Figure 1c) [*Assumpção et al.*, 2013]. An average thickness of ∼38 km is observed beneath the stable continental platform, apart from narrow belts surrounding the cratons of central Brazil, such as the Transbrasiliano lineament where crustal thickness is less than 35 km. One significant exception is the Borborema Plateau, where crustal thickness is 30–35 km. Along the Andean chain, crustal thickness is ∼75 km beneath the Central Andes, but values of ∼40 km have been reported for the Patagonian Andes and for the Northern Andes of Ecuador and Colombia, despite their considerable elevation.

Surface wave tomographic models have been used to determine changes in lithospheric thickness [e.g., *van der Lee et al.*, 2001; *Heintz et al.*, 2005; *Feng et al.*, 2007; *Rocha et al.*, 2011]. A narrow and fast velocity anomaly occurs at depths of 150–250 km beneath the western margin between 0°S and 30°S. This anomaly coincides with the position of the Nazca plate. The geometry of flat slab subduction beneath northern Colombia, western Peru, and central Chile is manifest by high S-wave velocities at a depth of 100 km. Extremely slow velocities occur at 100 km depth within the mantle wedge beneath the Altiplano and Eastern Cordillera. In contrast, fast velocities down to 150–200 km characterize the older, stable lithosphere beneath cratons.

Positive, long-wavelength (i.e., >730 km) non-hydrostatic free-air gravity anomalies coincide with elevated topography (Figure 1b) [*Chambat et al.*, 2010; *Mayer-Guerr,* 2015]. For example, an anomaly of +100 mGal is centered on the Central Andean Plateau. Along the eastern seaboard, a gravity anomaly of +30 mGal is centered on the Borborema Province. Smaller positive and negative anomalies with amplitudes of 10–20 mGal occur along the Atlantic margin between 20°S and 40°S. This pattern of anomalies is consistent with oceanic residual depth measurements, which suggests that regional elevation is not solely maintained by crustal isostasy (Figure 1b) [*Hoggard et al.*, 2017].

2.1 Crustal Isostasy

At shorter wavelengths (i.e., <100 km), regional topography is partially supported by elastic stresses within the lithosphere [e.g., *Watts*, 2001]. At longer wavelengths, the lithosphere can be dynamically supported by sub-plate density anomalies. To determine the degree to which topography is supported by subcrustal or sub-lithospheric processes, elevation can be isostatically balanced with respect to the mid-oceanic ridge system.

Figure 1c shows crustal and lithospheric thickness estimates across South America. Lithospheric thickness is calculated from a surface wave tomographic model [*Priestley and McKenzie,* 2013]. Crustal thickness measurements are taken from *Assumpção et al*. [2013]. Figure 1d summarizes the isostatic relationship between crustal and lithospheric measurements and elevation. The correlation between crustal thickness and elevation is generally poor and elevated areas can have anomalously thin crust. One example is the Borborema Province where crustal isostatic considerations suggest that elevation is >0.5 km greater than expected. Similar anomalies are evident in the Central Andean Plateau, where residual elevations of >1 km occur.

2.2 Admittance Analysis

The spectral relationship between free-air gravity anomalies and topography is used to determine the flexural rigidity of the lithospheric plate and the degree of long-wavelength dynamic support. First, the observed admittance, $Z(k)$, which is the ratio of free-air gravity and topography as a function of wavenumber, k, is determined for a region. Z is a measure of the degree of compensation and is often used to estimate T_e, the elastic thickness. Second, an inverse model finds the optimal T_e and estimates the percentage of subsurface loading [e.g., *McKenzie,* 2003]. This model seeks a value of T_e that minimizes the misfit between observed and calculated values of $Z(k)$. Deviations from the best-fitting model at the longest wavelengths are a manifestation of dynamic (i.e., sub-plate) support. Here, admittance analysis is carried out for two regions where free-air gravity anomalies and topographic relief have a high degree of coherence (Borborema

Province and Central Andean Plateau). Elsewhere in South America, a lack of topographic relief greatly reduces the value of this coherence and calculated values of T_e are much less reliable [*Tassara et al.*, 2007].

2.2.1 Borborema Province

The Borborema Province is a Precambrian domain located at the eastern edge of the Brazilian shield. It covers an area of 3.8×10^5 km² and is bound to the south by the São Francisco craton and to the west by the Parnaíba cratonic basin. This region is characterized by low relief mesas and plateaux with maximum elevations of about 1 km (Figure 2a). The most prominent physiographic feature is the Borborema Plateau, which has a roughly elliptical shape. The entire province underwent Late Cretaceous and, especially Cenozoic, epeirogenic uplift and volcanism [e.g., *Jardim de Sá et al.*, 1999; *Almeida et al.*, 2000; *Misuzaki et al.*, 2002; *Morais Neto et al.*, 2009; *Knesel et al.*, 2011; *Oliveira and de Medeiros*, 2012].
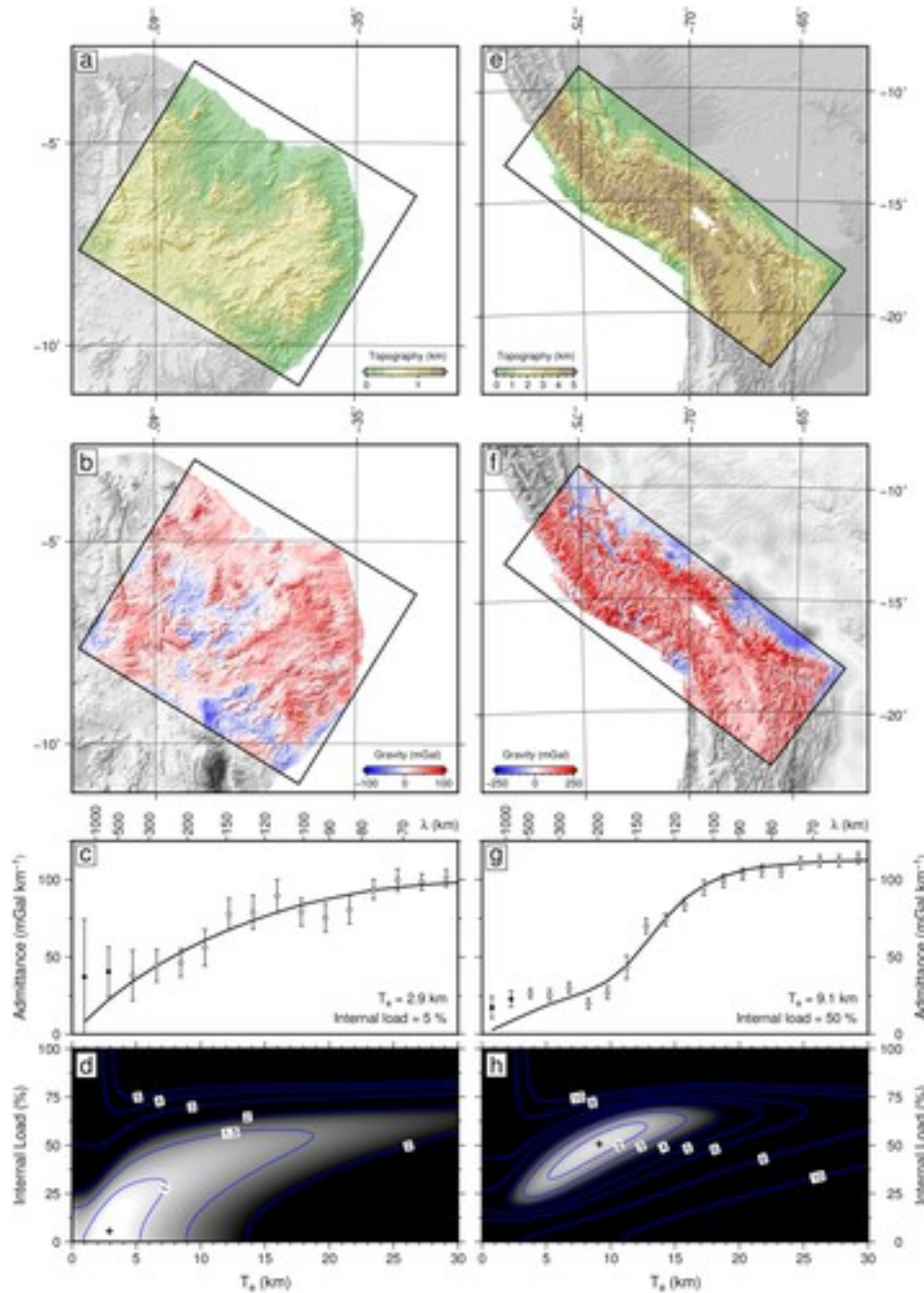
Figure 2
Open in figure viewerPowerPoint

(a) Topographic map of Borborema Plateau from SRTM30 _PLUS [*Becker et al.*, 2009]. (b) Free-air gravity anomalies from EIGEN-6C3stat data set plotted at 6 arc minute resolution [*Förste et al.*, 2013]. (c) Admittance, *Z*, as function of wavelength calculated from grids shown in Figures 2a and 2b. Solid/open circles with error bars = observed values of *Z* with $\pm 1\sigma$; solid line = best-fitting variation of *Z* calculated by fitting open circles with elastic thickness, T_e = 2.9 km and 5% internal loading [*McKenzie*, 2003]. Upper crustal thickness and density = 15 km and

2.40 Mg m^{-3}, respectively; lower crustal thickness and density = 15 km and 2.65 Mg m^{-3}, respectively. (d) Misfit between observed and calculated Z as function of T_e and internal loading with black cross at global minimum. (e) Topographic map of Central Andean Altiplano. (f) Free-air gravity anomaly of same area. (g) Admittance, Z, as function of wave number calculated from grids shown in Figures 2e and 2f. Solid/open circles with error bars = observed values of Z with $\pm 1\sigma$; solid line = best-fitting variation of Z calculated by fitting open circles with elastic thickness, T_e = 9.1 km and 50% internal loading [*McKenzie*, 2003]. Upper crustal thickness and density = 45 km and 2.70 Mg m^{-3}, respectively; lower crustal thickness and density = 15 km and 2.80 Mg m^{-3}, respectively. (h) Misfit between observed and calculated Z as function of T_e and internal loading with black cross at global minimum.

[Caption]

Numerous mechanisms have been proposed to account for Cenozoic epeirogenic uplift of the Borborema Province. These mechanisms include: passage of South America over a deep-seated mantle plume that currently sits beneath Fernando de Noronha [*Jardim de Sá et al.*, 1999]; thermal doming caused by anomalously hot shallow mantle [*Ussami et al.*, 1999]; lithospheric erosion generated by an edge-driven convection cell [*Knesel et al.*, 2011]; magmatic underplating [*Oliveira and de Medeiros*, 2012]; and, finally, lithospheric thickening and thermal re-equilibration triggered by lithospheric flow during Mesozoic extension [*Morais Neto et al.*, 2009].

A deep-seated convective plume is not generally favored for several reasons. First, there is little evidence for a systematic spatio-temporal pattern of onshore and offshore volcanism. The volume of basaltic magmatism is small and its distribution is characterized by long-lived and overlapping activity throughout the Borborema Province and Fernando de Noronha [*Knesel et al.*, 2011]. A slow seismic velocity anomaly has not been imaged beneath Fernando de Noronha [e.g., *Courtillot et al.*, 2003]. Receiver function analyses from the Borborema Plateau suggest that upper mantle transition zones are not thermally deflected [*Pinheiro and Julià*, 2014]. Clearly, thin crust occurs beneath elevated portions of the Borborema plateau, suggestive of some degree of sub-plate thermal support [*Almeida et al.*, 2015].

$Z(k)$ is calculated for a box that encompasses the Borborema Province using the EIGEN-6C gravity and SRTM30-plus topographic databases (Figures 2a–2d) [*Becker et al.*, 2009; *Förste et al.*, 2013]. Upper and lower crusts are assigned thicknesses of 15 km and densities of 2.40 and 2.65 Mg m^{-3}, respectively. The misfit between observed and calculated admittance is minimized by sweeping through T_e = 0–30 km for different percentages of internal loading. A global minimum is located at T_e = 2.9 km with minor internal loading. This value of T_e is consistent

with $T_e < 25 \pm 15$ km reported by *Tassara et al*. [2007], who analyzed the coherence between Bouguer gravity anomalies and topography using wavelet techniques. At wavelengths of greater than 500 km, $Z \rightarrow 40 \pm 15$ mGal km⁻¹. This observation is entirely consistent with shallow dynamic convective support [*McKenzie*, 2010; *Colli et al*., 2016]. A small box size means that the internal load fraction is indistinguishable from zero and that the value of $Z(k)$ at long-wavelengths is uncertain [*Crosby*, 2007]. We conclude that plateau elevation cannot be supported by flexural rebound associated with unloading at the adjacent deep-water margin.

2.2.2 Central Andean Plateau

The Central Andean Plateau is ~1800 km long, reaching from southern Peru to northern Argentina with a width of 350–450 km. The Altiplano and Puna subdomains are located at the center of the Central Andean Plateau and comprise elevated areas of low relief flanked by numerous cordillera [*Isaks*, 1988; *Allmendinger et al*., 1997]. Different uplift mechanisms have been proposed that include: crustal shortening [e.g., *Isaks*, 1988; *McQuarrie*, 2002]; changes in subducting plate geometry [e.g., *Allmendinger et al*., 1997; *Hoke and Lamb*, 2007]; cratonic underthrusting [*Lamb and Hoke*, 1997]; magmatic underplating [*Kono et al*., 1989], delamination [e.g., *Lamb and Hoke*, 1997; *Garzione et al*., 2006; *Schildgen et al*., 2007]; crustal flow [*Husson and Sempere*, 2003; *Thouret et al*., 2007]; and coupling of tectonic processes and climate-driven erosion [e.g., *Barnes and Pelletier*, 2006; *Strecker et al*., 2007; *McQuarrie et al*., 2008b].

The Central Andean Plateau is characterized by positive long-wavelength free-air gravity anomalies and by elevated heat flow (Figures 1b and 2f) [*Götze and Kirchner*, 1997; *Hamza et al*., 2005]. Seismic wide-angle experiments and receiver function analyses yield crustal thicknesses of 30–38 km in the foreland zones and 80 km beneath the Western and Eastern Cordilleras [*Zandt et al*., 1994; *Beck et al*., 1996; *Beck and Zandt*, 2002; *Yuan et al*., 2002; *Assumpção et al*., 2013]. Beneath the northern Altiplano, the crust is 60–70 km thick. Along the Altiplano-Eastern Cordillera zone, the crust thins southward and is 50 km thick beneath the Puna subdomain south of 22°S [*Beck et al*., 1996; *Beck and Zandt*, 2002; *Yuan et al*., 2002].

Imaging of lithosphere structure has yielded less obvious conclusions (see compilation of *Barnes and Ehlers* [2009]). The geometries of the subducting Nazca plate and of underthrust Brazilian cratonic lithosphere are better imaged. In some cases, a region of fast velocity beneath the Altiplano that thins toward the Puna subdomain has been identified. This observation may reflect piecemeal delamination of lithospheric mantle. Seismic anisotropic studies reveal a N-S orientation of shear-wave splitting directly below the Altiplano that might be related to mantle

flow [*Bock et al.,* 1998; *Polet et al.*, 2000]. This orientation contrasts with a zone of W-E fast orientation east of 66°W that is interpreted as Brazilian lithosphere.

We calculate $Z(k)$ for a box encompassing the northern Central Andean Plateau (Figures 2e and 2f). Upper and lower crustal thicknesses are 15 and 45 km with densities of 2.7 and 2.8 Mg m^{-3}, respectively. A global minimum occurs at $T_e = 9.1$ km with an internal load of 50%. Given the level of uncertainty, this value of T_e is consistent with $T_e < 15$ km obtained by analysis of the coherence between Bouguer gravity anomalies and topography [*Tassara et al.,* 2007]. At wavelengths >1000 km, $Z \rightarrow 23 \pm 5$ mGal km^{-1}, which is consistent with some degree of dynamic convective support.

3 Drainage Analysis

Analysis of ubiquitous drainage networks might prove useful in complementing spot measurements of regional uplift that necessarily have limited spatial coverage. These networks set the pace of denudation, and there is renewed interest in exploring how they can be used to quantify spatial and temporal patterns of regional uplift. In short, do longitudinal river profiles act as tectonic "tape recorders"? Here, we attempt to answer this question by modeling a continent-wide drainage inventory.

We extract 1827 river profiles of Strahler order ≥ 5 from a digital elevation model generated from a 3 arc second (i.e., 90×90 m^2) Shuttle Radar Topographic Mission (SRTM) database [*Farr et al.,* 2007]. First, anomalous spikes and sinks from the digital topography are excised. Second, flow-routing algorithms from the ArcGIS software package are used to calculate drainage networks (Figures 3a and 3b) [*Tarboton,* 1997]. The fidelity of these networks is verified using Landsat imagery (Figures 3c and 3d). Finally, longitudinal river profiles (i.e., elevation as function of distance along a river channel) are extracted.
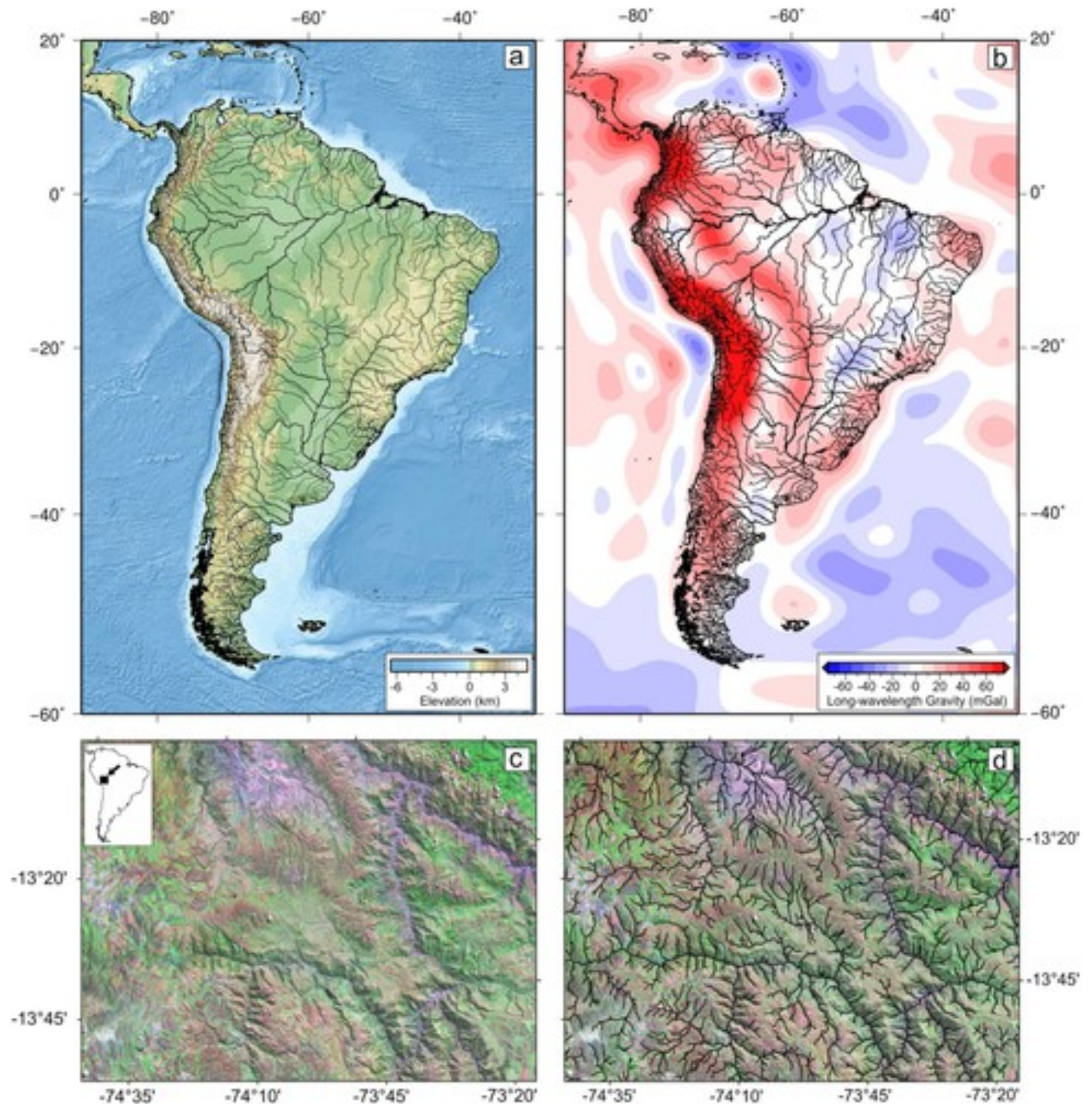
Figure 3
(a) Topographic map of South America overlain with drainage network comprising 1827 rivers extracted from Shuttle Radar Topography Mission (SRTM) data set. (b) Long-wavelength (> 730 km) non-hydrostatic free-air gravity anomaly map overlain with drainage network [*Mayer-Guerr*, 2015]. (c) Landsat satellite image from Central Peruvian Andes showing drainage network. Inset shows location. (d) Same image as Figure 3c overlain with recovered drainage network.

It is reasonable to assume that the present-day drainage pattern of South America was configured after separation from Africa in Early Cretaceous times. At the present-day, the bulk of rivers drain into either the southern Atlantic Ocean or the Caribbean Sea [*Potter*, 1997; *Lundberg et al.*, 1998]. Most of the low relief continental interior is drained by long, meandering river networks. In contrast, the Borborema and Araripe Plateaux, the Pakaraima Mountains of the Guyana Shield, and the southern Patagonian Plateau have radial drainage patterns. Finally, the Andean Cordillera is characterized by short and steep rivers that drain directly into the adjacent Pacific Ocean (Figure 3).

3.1 Modeling Strategy

The shapes of river profiles at long-wavelengths appear to be moderated by a combination of uplift rate, *U*, and erosion rate, *E*, both of which can vary as a function of time and space [e.g., *Whipple and Tucker*, 1999]. The rate of change in elevation along a river profile, $\partial z / \partial t$, can therefore be described by

$$-\frac{\partial z}{\partial t} = U(x,t) + E(x,t), \quad (1)$$

where *z* is elevation along the profile, *t* is time before present-day, and *x* is distance from the mouth of the river. Erosional processes can be approximated by two terms. The first term consists of headward propagation of steep slopes (i.e., detachment-limited erosion) [*Howard and Kerby*, 1983; *Whipple and Tucker*, 1999]. The second term constitutes downwearing caused by sedimentary transport (i.e., transport-limited erosion) [*Rosenbloom and Anderson*, 1994; *Sklar and Dietrich*, 1998, 2001; *Whipple and Tucker*, 1999; *Tomkin*, 2003]. In this way, an empirical stream-power formulation is written as

$$E(x,t) = -v_o [PA(x)]^m \left(\frac{\partial z}{\partial x}\right)^n + \kappa \frac{\partial^2 z}{\partial x^2}, \quad (2)$$

where v_o is the advective (i.e., knickpoint retreat) constant that has the dimensions of velocity when $m = 0$ and $n = 1$, *P* is precipitation rate, *A(x)* is present-day upstream drainage area, and κ is "erosional diffusivity." *n* and *m* are dimensionless erosional constants that affect profile concavity [*Whipple and Tucker*, 1999; *Roe et al.*, 2002]. For a given profile and appropriately chosen erosional parameters, it is feasible to invert for uplift rate by minimizing the misfit between observed and calculated river profiles. *Pritchard et al.* [2009] and *Roberts and White*[2010] demonstrate that individual river profiles can be linearly or non-linearly inverted by varying uplift rate history as a function of time alone. Subsequently, *Roberts et al.* [2012a] developed a non-linear optimization scheme that permits substantial inventories of river profiles to be simultaneously inverted by varying uplift rate history as a function of both time and space. This general scheme has been successfully applied to different continents and suggests that the empirical stream-power formulation provides a practical basis by which patterns of regional uplift through space and time can be assessed [*Roberts et al.*, 2012b; *Czarnota et al.*, 2014; *Paul et al.*, 2014; *Wilson et al.*, 2014; *Stephenson et al.*, 2014; *Richards et al.*, 2016].

Any such optimization scheme depends upon the values of erosional parameters. Estimates of v_o , m, κ and especially n are difficult to obtain and are much debated [e.g., *van der Beek and Bishop*, 2003; *Royden and Perron*, 2013; *Lague*, 2014]. Previous analysis has shown that varying the values of these parameters affects the residual misfit between observed and calculated river profiles in different ways [*Pritchard et al.*, 2009; *Roberts and White*, 2010; *Roberts et al.*, 2012a, 2012b; *Czarnota et al.*, 2014; *Paul et al.*, 2014]. *Roberts and White* [2010] and *Croissant and Braun* [2014] show that v_o and m trade off negatively so that different combinations of m and v_o can yield equally good fits. Nonetheless, optimal values of m alone can be identified by examining the misfit between observed and predicted rivers. v_o sets the timescale for knickpoint retreat. An optimal combination of m and v_o values is identified by independent calibration. *Pritchard et al.* [2009] and *Royden and Perron* [2013] argue that for values of $n > 1$ shock wave behaviour develops along trunk rivers and their tributaries, so that steeper slopes travel faster than shallower slopes. If so, knickzone retreat could potentially erase portions of uplift rate histories since reconstructed records would contain spatiotemporal gaps. *Pritchard et al.* [2009] assert that $n \sim 1$ since there is little direct observational evidence for shock waves. *Paul et al.* [2014] and *Czarnota et al.* [2014] show that a global minimum occurs at, or near, $n = 1$. The locus of this minimum does not appear to vary for different degrees of discretization or smoothing. *Rosenbloom and Anderson* [1994] suggest that κ is probably less than 5×10^5 m² Ma⁻¹. However, κ can vary by many orders of magnitude without affecting results (e.g., 1–10⁷ m²Ma⁻¹).

These modeling strategies generally assume that P and A are invariant. Obviously, A can vary due to migration of drainage divides and river capture events, which are not specifically incorporated in inversion schemes although the effect of changing A has been investigated [*Paul et al.*, 2014]. P undoubtedly varies through space and time. Significantly, however, the integral solution of equation 1 indicates that large excursions in A and P have a minor effect on recovered uplift rate histories. *Paul et al.* [2014] and *Wilson et al.* [2014] show that misfit between observed and calculated river profiles varies weakly with A since it is taken to a fractional power (i.e., m). Recovered uplift rate histories remain essentially unchanged when precipitation rate varies with a periodicity of less than several million years. Thus periodic precipitation variation caused by, say, orbital cyclicity demonstrably does not alter the long-wavelength shapes of river profiles [*Paul et al.*, 2014]. Similarly, glacioeustatic fluctuations of sea level are too rapid to significantly affect the long-wavelength shapes of river profiles. Finally, slope and curvature of river profiles only weakly correlate with lithologic contrasts at wavelengths larger than several kilometers.

3.2 Landscape Response Time

It is helpful to determine how rapidly longer wavelength knickzones propagate upstream with time using an approach based upon *Weissel and Seidl* [1998]. If $\kappa = 0$ and $n = 1$, the time, τ_G, taken for a knickzone inserted at the mouth of the river to arrive at a given position, x, along the river channel is given by

$$\tau_G = \int_0^x \frac{dx}{vA(x)^m},$$
(3)

where τ_G is Gilbert time (i.e., landscape response time). τ_G is an estimate of how far back in time river channels can potentially record uplift rate histories (Figure 4b). Short rivers at coastal areas can potentially record uplift events of Neogene age or younger. In contrast, long rivers flowing across low-lying cratonic areas are sensitive to older events. For the bulk of South America, we suggest that reliable uplift histories can be recovered for the last ~35 Ma. Close to drainage divides, $\tau_G \rightarrow \infty$ as A approaches zero. Juxtaposition of significantly different values of τ_G (or its dimensionless equivalent χ) on either side of drainage divides have been used to infer divide migration toward the catchment with the higher value of τ_G [*Willett et al.*, 2014]. Unfortunately, values of τ_G are merely an indication of the time taken for a notional knickzone that is inserted at a river mouth to travel up to the river source. Since regional uplift patterns vary spatially, knickzones are often inserted at upstream loci which means that they reach the river source in a shorter time. Consequently, juxtaposition of different values of τ_G has no particular physical meaning and we caution against overinterpreting the spatial variation of τ_G in this way [*Willett et al.*, 2014].
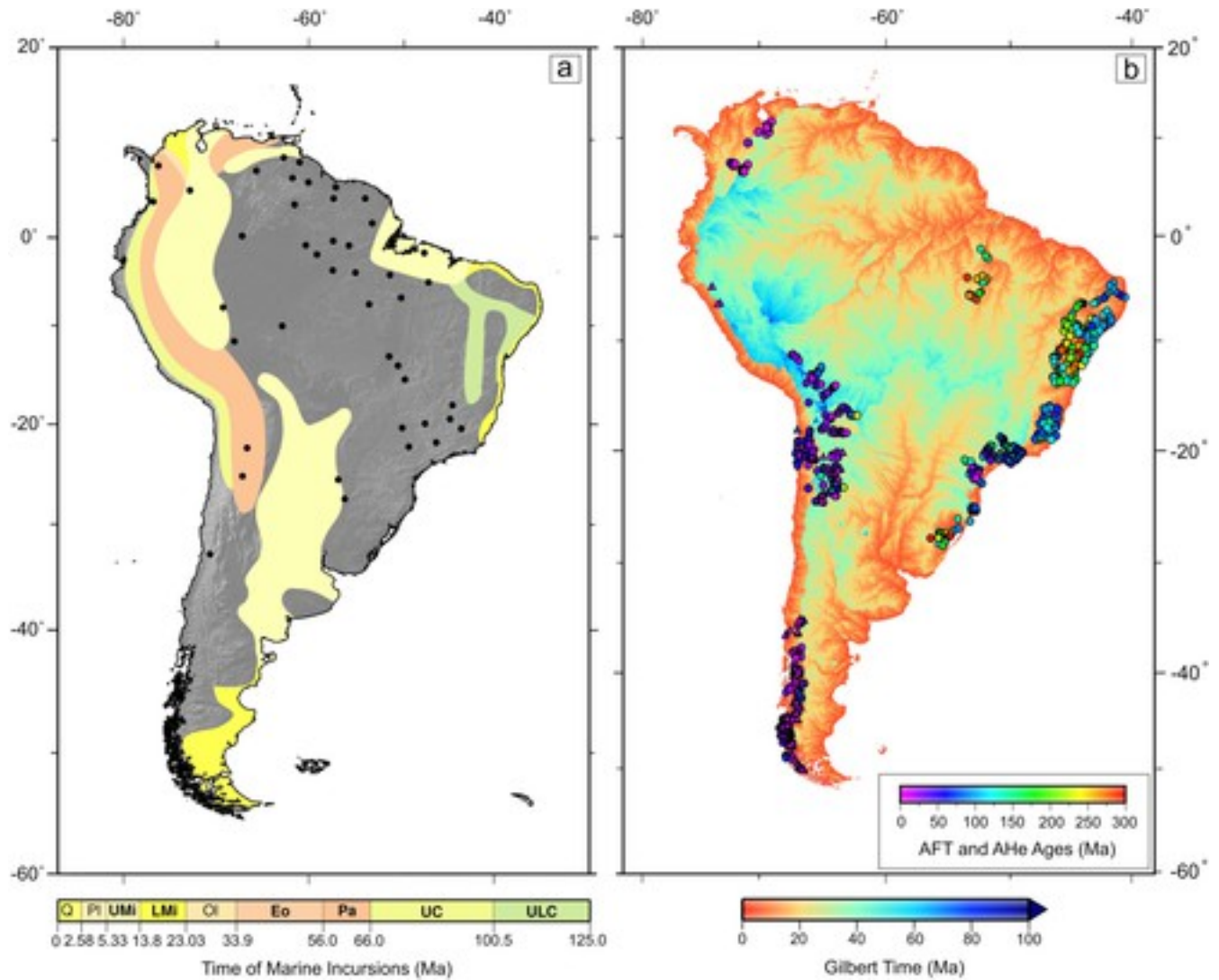
Figure 4
Open in figure viewerPowerPoint

(a) Schematic Cenozoic and Mesozoic paleogeographic map of South America. Colored polygons = age and extent of post-Mesozoic marine incursions from distribution of marine and coastal strata [after *Lundberg et al.*, 1998; *Arai*, 2014]; black circles = bauxite/laterite deposits [after *Lima da Costa*, 1993]. (b) Landscape response time, τ_G, calculated from digital elevation model using equation 3 with $m = 0.35$ and $v = 10$. Colored circles/triangles = AFT and A-He ages (*Restrepo-Moreno et al.* [2009]; *Parra et al.* [2009]; *Bermúdez et al.* [2010, 2011]; *Villagómez et al.* [2011]; *Michalak et al.* [2016] for the Northern Andes; selected references from compilation in *Barnes and Ehlers* [2009] for Central Andes; *Thomson et al.* [2001, 2010]; *Haschke et al.* [2006]; *Guillaume et al.* [2013] for Southern Patagonian Andes; and *Gallagher et al.* [1994]; *Harman et al.* [1998]; *Hackspacher and Ribeiro* [2004]; *Turner et al.* [2008]; *Morais Neto et al.* [2009]; *Franco-Magalhaes et al.* [2010, 2014]; *Hiruma et al.* [2010]; *Cogné et al.*

[2011, 2012]; *Japsen et al.* [2012]; *Jelinek et al.* [2014]; *Oliveira et al.* [2016] for South American Platform).

Caption

4 Uplift Through Space and Time

Our aim is to estimate spatial and temporal patterns of regional uplift by simultaneously inverting an inventory of 1827 river profiles (Figure 3). For simplicity, we assume that South America was low-lying with negligible relief in Early Cenozoic times. This assumption is supported by two sets of observations (Figure 4a). First, relics of Cretaceous-Cenozoic marine sedimentary rocks crop out across the continent and show that marine incursions affected large regions at different times [*Lovejoy et al.*, 1998; *Lundberg et al.*, 1998; *Arai*, 2000; *Hernández et al.*, 2005; *Arai*, 2014]. Second, lateritic and bauxitic deposits crop out on elevated, low-relief plateaux [*Prasad*, 1983; *Bárdossy and Aleva*, 1990; *Lima da Costa*, 1993]. These plateaux are regarded as remnants of erosional peneplains that developed during periods of tectonic quiescence and were subsequently uplifted and incised [e.g., *McConnell*, 1968; *Briceño and Schubert*, 1990; *Peulvast and de Claudino Sales*, 2004; *Peulvast et al.*, 2008; *Japsen et al.*, 2012; *Bétard et al.*, 2014; *Peulvast and Bétard*, 2015]. Abundant deposits occur on the Guyana Shield, within the Amazon Basin, and on the Brazilian Shield (Figure 4a) [*Bárdossy and Aleva*, 1990; *Lima da Costa*, 1993].

Many lateritic horizons rest on Precambrian metamorphic and igneous rocks. However, along the coastal plains of Suriname, abundant Eocene-Oligocene duricrusts developed on top of Paleocene deposits that were subsequently covered by Miocene marine sedimentary rocks. The thickness of these duricrusts is indicative of intense chemical weathering [*Prasad*, 1983; *Bárdossy and Aleva*, 1990]. A number of absolute dating studies have been carried out in the Carajás region of northeast Brazil and in the Quadrilátero Ferrífero region of southeast Brazil [*Vasconcelos et al.*, 1994; *Ruffet et al.*, 1996; *Spier et al.*, 2006]. Analysis of manganese oxides suggests that these deposits were precipitated between 50 and 40 Ma, consistent with low relief and tectonic quiescence during Paleogene times.

4.1 Linear Inverse Modeling

The linear inverse problem is based upon a simplified version of equation 1, such that

$$-\frac{\partial z}{\partial t} + vA^m \frac{\partial z}{\partial x} = U(x, t). \tag{4}$$

Rudge et al. [2015] solve this equation using the method of characteristics [e.g., *Lighthill and Whitham*, 1955; *Weissel and Seidl,* 1998]. The linear inverse problem is posed in which an inventory of river profiles (i.e., a collection of (*x*,*y*,*z*) points along a large number of rivers) is used to retrieve uplift rate as a function of space and time. In order to achieve this end, it is first necessary to discretize the problem in both time and space. Temporal discretization is carried out by setting the number of time intervals at which uplift rate is calculated. The land surface is discretized using a triangular mesh. As a result, a set of spatial and temporal vertices is defined at which uplift rate is allowed to vary during inversion. Values of uplift between nodes are obtained by linear interpolation. The inverse problem is then solved by implementing a damped, non-negative, least squares (NNLS) algorithm [*Rudge et al*., 2015]. This algorithm minimizes the misfit between observed and calculated rivers using

$$|\mathbf{MU}-\mathbf{z}|^2 + \lambda_S^2 |\mathbf{SU}|^2 + \lambda_T^2 |\mathbf{TU}|^2 \tag{5}$$

subject to $\mathbf{U} \geq 0$, where $\mathbf{z}$ is a set of elevations at different positions along river profiles, $\mathbf{U}$ is a set of uplift rate values at different spatial and temporal nodes, and M is a matrix that defines the relationship between distance and time. λ_S and λ_T are spatial and temporal smoothing parameters that control regularization of this inverse problem. The matrix S describes spatial smoothing according to

$$|\mathbf{SU}|^2 = \int_S \int_{t=0}^{t_{max}} |\nabla U|^2 \, dt \, dS, \tag{6}$$

where t_{max} is the maximum Gilbert time.

The matrix T describes temporal smoothing according to

$$|\mathbf{TU}|^2 = \int_S \int_{t=0}^{t_{max}} \left| \frac{\partial U}{\partial t} \right|^2 \, dt \, dS. \tag{7}$$

Optimal values of λ_S and λ_T are chosen by seeking the smoothest model that yields a minimum misfit between observed and calculated river profiles [*Parker*, 1994]. In this study, we use $\lambda_T = 1$ and $\lambda_S = 0.36$, for $v = 10$ and $m = 0.35$.

Figure 5 shows observed and calculated river profiles for 6 major catchments. Residual misfits are 0.50–7.55, the largest residual misfit being for the Magdalena Basin. The average residual misfit for the continent-wide drainage inventory of 1827 river profiles is 4. The ability to fit large numbers of river profiles suggests that drainage networks are recording coherent topographic signals through time and space when kinematic waves of incision propagate through the landscape. The resultant cumulative uplift history (i.e., $\int_0^t U(x, y, t) \, dt$) is shown in Figure 6. This history suggests that the bulk of South American topography grew during Cenozoic times. Andean uplift started in Late Eocene-Oligocene (40–28 Ma) times and increased rapidly during Miocene times when this mountain chain was created. Earlier uplift occurred in the northern

Andes of Venezuela and Colombia between 40 and 24 Ma. The rest of the northern Andes, together with southern and central portions of the mountain chain, underwent post-Oligocene (i.e., <28 Ma) uplift.
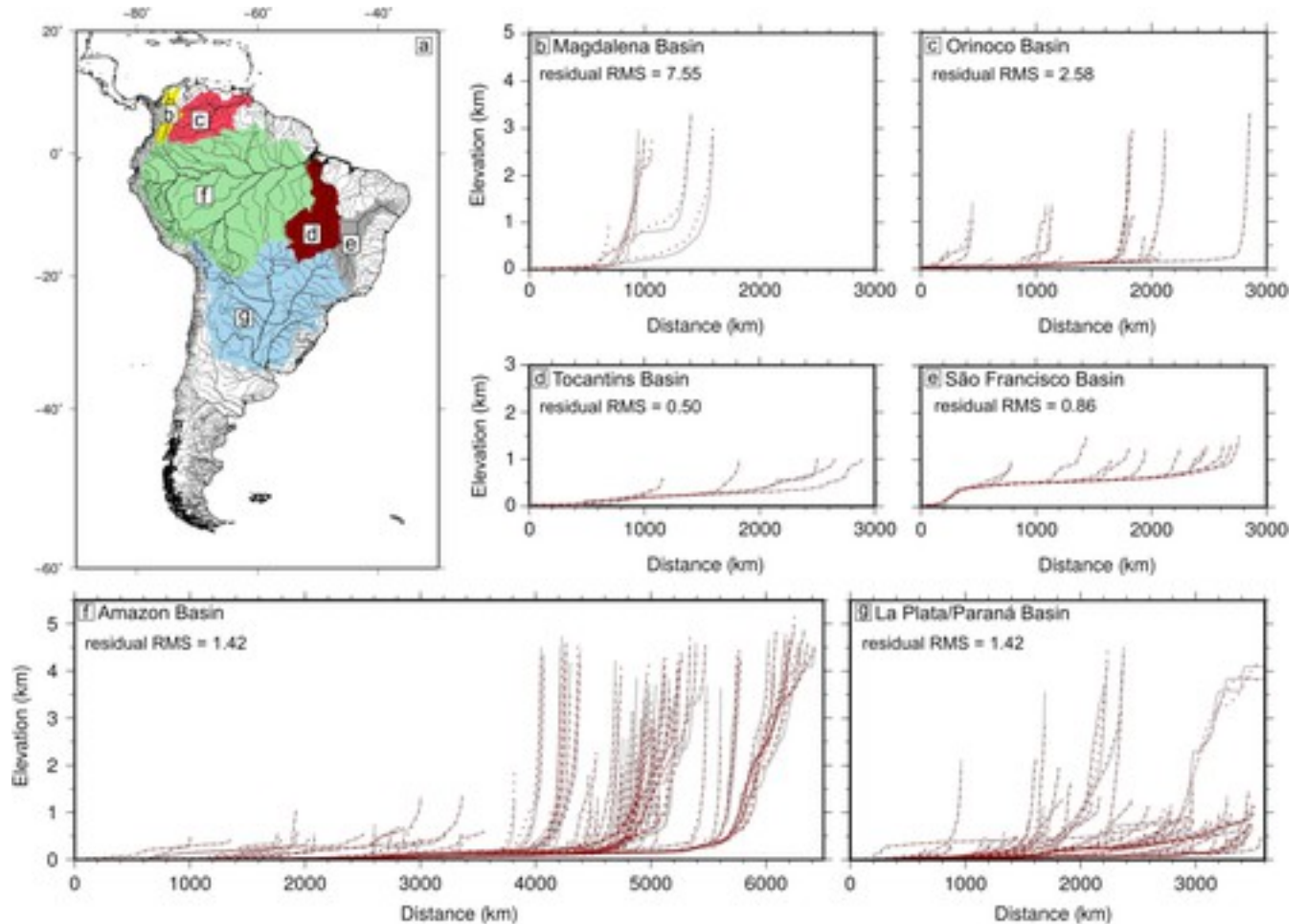

Figure 5

Inverse modeling of 1827 South American river profiles. (a) Drainage map. Colored polygons = six largest catchments, where labels correspond to Figures 5b–5g. (b)–(g) Gray/red lines = observed and calculated river profiles, respectively. In each case, residual RMS misfit for the catchment is given.

Caption

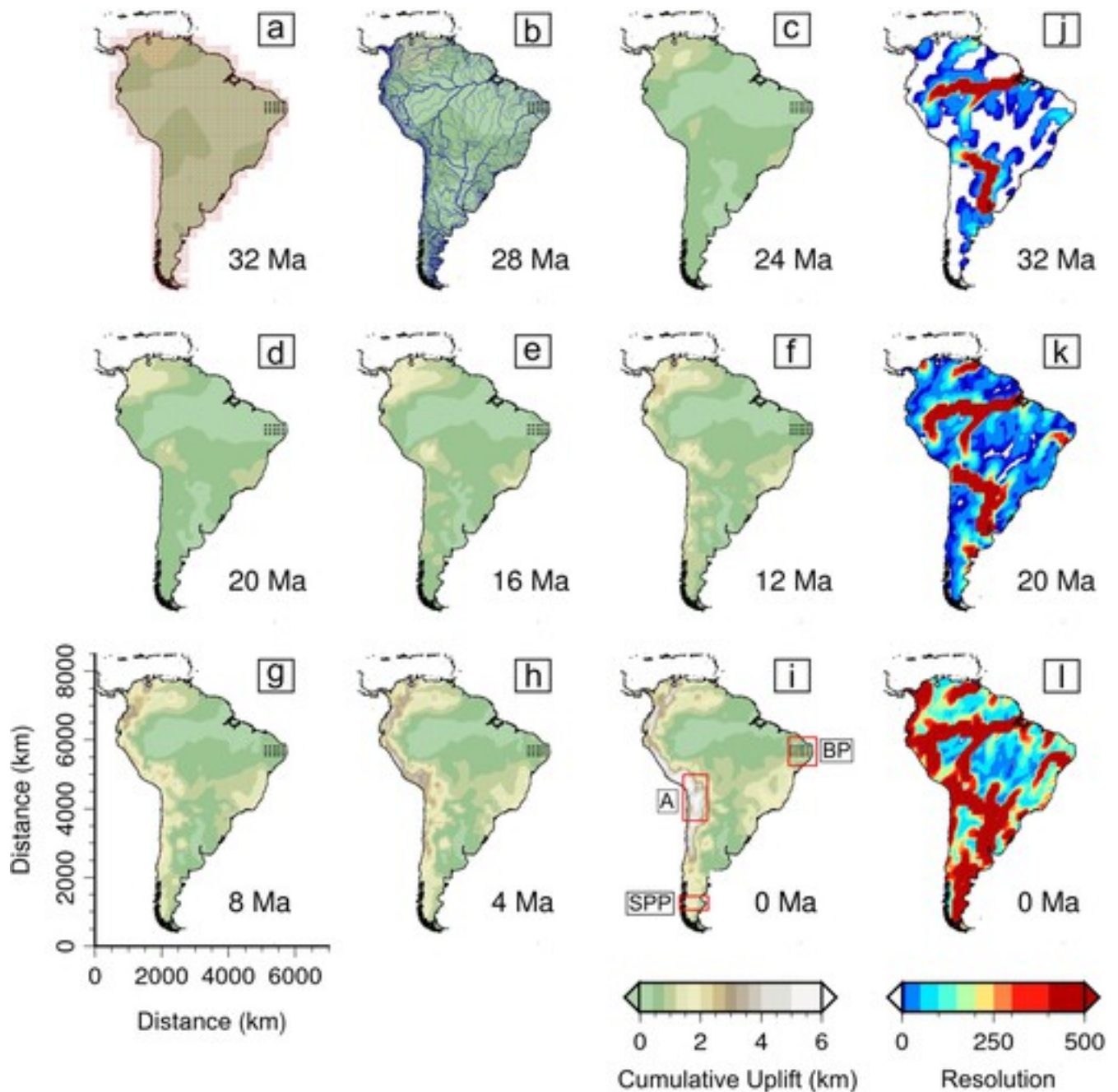**Figure 6**
Calculated cumulative uplift history of South America (i.e., $\int_0^t U(x,y,t)\,dt$) as function of space and time. (a) Cumulative uplift at 32 Ma. Red circles = spatial distribution of grid points at which uplift rate can vary during inversion. Black dots = nodes from Borborema Province where erosional parameters were calibrated. (b) Cumulative uplift at 28 Ma. Blue lines = 1827 river profiles used for inverse modeling. (c)–(i) Snapshots of cumulative uplift from 24 Ma to present-day. BP = Borborema Province; A = Central Andean Altiplano; SPP = Southern Patagonian

Plateau. (j)–(l) Selected plots at three different times showing number of nonzero entries in model matrix, *M,* for given uplift nodes.

Caption

4.2 Calibration of Erosional Parameters

An ability to recover realistic uplift histories depends upon the choice of erosional parameters *v* and *m* that determine the speed at which kinematic waves of incision sweep through the eroding landscape. Although *v* and *m* negatively trade off against each other, they can be considered separately since the value of *v* does not directly affect the quality of the fit between observed and calculated river profiles, whereas the value of *m* does. To determine the optimal value of *m,* we invert the drainage inventory multiple times using different values of *m* that vary between 0 and 1 in steps of 0.05. The variation of residual misfit as a function of *m* is shown in Figure 7. A shallow global minimum occurs at $m = 0.4 \pm 0.05$ for $\lambda_S = 0.36$ and $\lambda_T = 1$, which broadly agrees with the published range of estimates [e.g., *Schoenbohm et al.,* 2004].
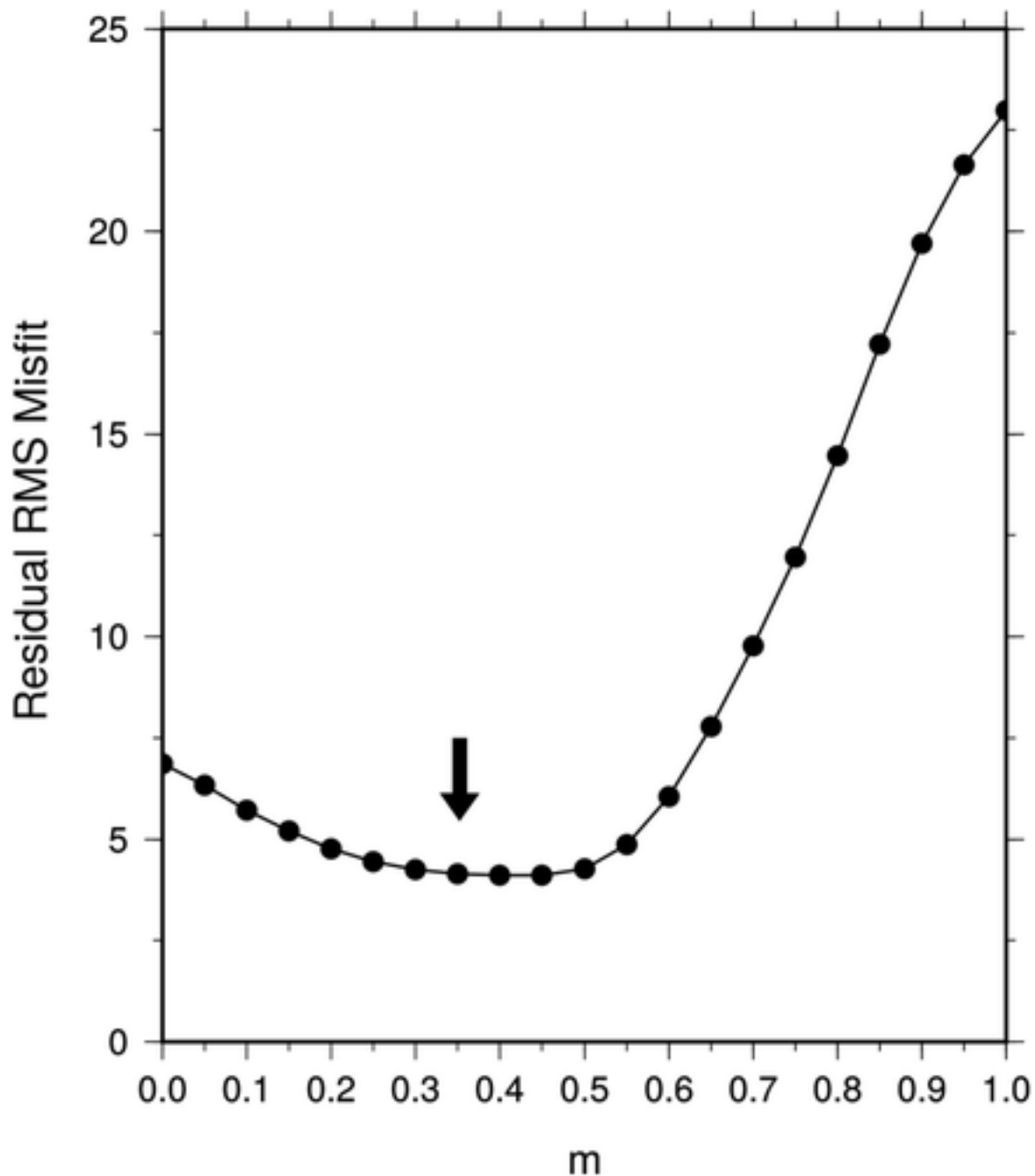
Figure 7
Residual RMS misfit between observed and calculated river profiles plotted as function of *m*.
Arrow = optimal value of $m = 0.35$. Note shallow global minimum at $m = 0.3$–0.5.

Caption
The value of *v* directly determines the timescale of recovered uplift rate history. If *v* is small,
waves of incision travel more slowly through the landscape. Recovered uplift rate is therefore
distributed over a longer period. For larger values of *v*, recovered uplift rates are distributed over

shorter periods. Here, we calibrate v using independent geologic observations of regional uplift from the Borborema Province in northeast Brazil (Figure 8).
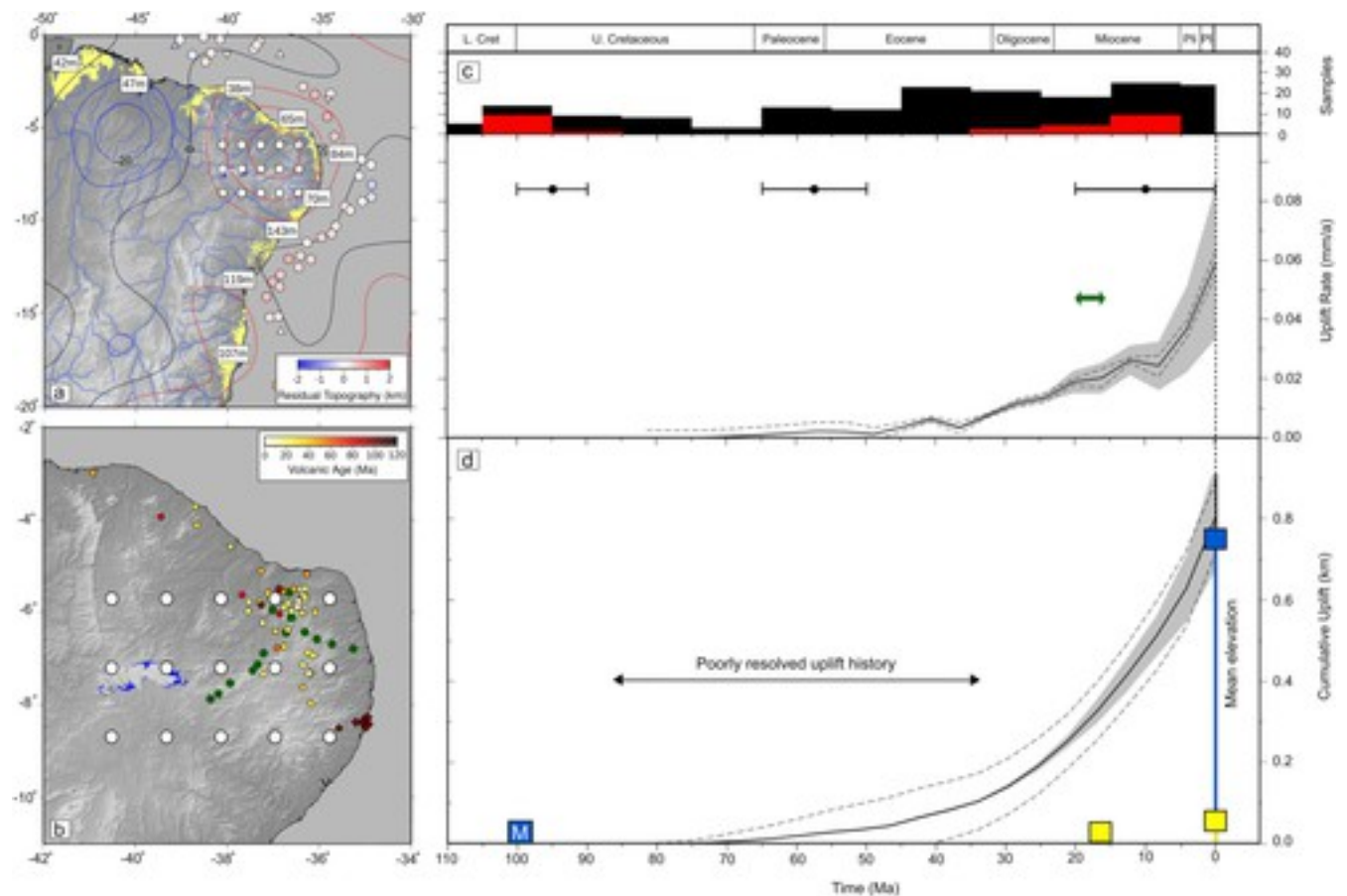

Figure 8

Uplift history of Borborema Province. (a) Topographic map. Colored circles and upward/downward triangles = offshore estimates and lower/upper limits of residual depth anomalies [*Hoggard et al.*, 2017]; red/black/blue contours = positive/zero/negative long-wavelength (>730 km) nonhydrostatic gravity anomalies [*Mayer‑Guerr*, 2015]; thin blue lines = river profiles; labeled yellow polygons = shallow marine/coastal Oligo‑Miocene Pirabas and Barreiras Formations with mean elevations [*CPRM‑Serviço Geológico do Brasil*, 2004; *Rossetti et al.*, 2013]; dark blue polygons = shallow marine fossiliferous limestones of Albian Santana Formation from Araripe Plateau [modified from *Assine*, 2007]; white circles = loci of nodes whence uplift rate and cumulative uplift histories are extracted. (b) Topographic map. Green circles = loci of apatite fission track analyses [*Morais Neto et al.*, 2009]; yellow/orange/red diamonds/circles = dated volcanic rocks (diamonds = $^{40}Ar/^{39}Ar$ ages from *Souza et al.* [2003, 2013]; *Nascimento et al.* [2003]; *Knesel et al.* [2011]; circles = K-Ar ages from *Misuzaki et al.* [2002]); white circles = loci of nodes; dark blue polygons = Santana Formation. (c) Black

line with gray band = average predicted uplift rate history with $\pm 1\sigma$ for nodes shown in Figure 8a where dashed lines show changes obtained by covarying *v* and *m* within ranges $5 \leq v \leq 18$ and $0.325 \leq m \leq 0.375$; histogram = magmatic samples (red bars = ^{40}Ar/^{39}Ar ages, black bars = K-Ar ages); solid circles with horizontal error bars = timings of exhumation events from thermochronologic studies; green arrow = start of increased clastic input into offshore basins (Potiguar, Pernambuco and Sergipe-Alagoas Basins) [*Pessoa Neto et al*., 2007; *Córdoba et al.,* 2007; *Campos Neto et al*., 2007]; (d) Black line with gray band = average predicted cumulative uplift history for node shown in Figure 8a; blue squares = original and present-day elevation of sedimentary rocks of shallow marine Santana Formation [*Morais Neto et al.,* 2009; *Pedoja et al.,* 2011b]; yellow squares = original and present-day elevation of coastal Barreiras Formation.

[Caption](#)

4.2.1 Uplift History of Borborema Province

It is recognized that this region has been affected by phases of Late Cretaceous and Cenozoic uplift. The most compelling evidence favoring youthful uplift is the distribution of Albian limestones of the Santana Formation that cap the Araripe Plateau and sit at an elevation of 700–800 m (Figures 8a and 8b) [*Morais Neto et al*., 2009]. These shallow water deposits have an abundant and diverse fauna (e.g., fish, mollusks, dinoflagellates, foraminifera, ostracods) [*Arai,* 2000, 2014; *Assine,* 2007]. They are remnants of the post-rift sequence of the Araripe basin, one of the largest intracontinental basin that formed during opening of the adjacent ocean [*Assine,* 2007]. Correlative deposits of the Santana Formation occur at an elevation of 600 m within the Reconcavo-Tucano-Jatobá basin located further south [*Magnavita et al.,* 1994].

Cenozoic strata, originally deposited closer to sea level, now crop out at elevation across the Borborema Province. In the northern part of this province, mesas with altitudes of 500–760 m are capped by coarse-grained sandstones and conglomerates of the Serra do Martins Formation, deposited between 64 and 25 Ma [*Morais Neto et al*., 2008, 2009]. At the coast, Oligo-Miocene marine strata are exposed along a narrow belt that is 5000 km long [*Rossetti et al*., 2013]. These strata comprise the Pirabas and Barreiras Formations and are exposed in discontinuous sea cliffs and river valleys. The Pirabas Formation is exposed between 4°N and 3°S and consists of mixed carbonate and siliciclastic deposits. It has a rich faunal content that includes shark fragments, gastropods, bivalves, ostracods as well as benthic and planktonic foraminifera [*Costa et al.,* 2004; *Ramos et al.,* 2004; *Távora et al.,* 2004]. Paleoenvironmental studies suggest a marine influence with deposition along the inner shelf, evolving toward a more lagoonal or estuarine environment [e.g., *Góes et al.,* 1990]. The Barreiras Formation occurs between 2°N and 22°S. It

is non-fossiliferous and comprises sandstones, mudstones, and conglomerates. Palynologic debris suggests that this formation is of Early to Middle Miocene age [*Leite*, 2004]. It is often stated that the Barreiras Formation is continental and that it is genetically unrelated to the Pirabas Formation [e.g., *Vilas Bôas et al.*, 2001; *Lima et al.*, 2006]. Recent analysis of deposits from both the equatorial and the eastern margins suggest that the Barreiras Formation shows influence of tidal processes, implying a closer depositional relationship between the two formations [*Góes et al.*, 1990; *Rossetti*, 2004; *Rossetti and Góes*, 2009; *Rossetti et al.*, 2012a]. Depositional structures suggestive of marine influence within the Barreiras Formation include bidirectional/herringbone cross-stratification, mud drapes, and mantled foresets. Ichnofossils typical of high energy, shallow marine environments are also found
[e.g., *Ophiomorpha, Diplocraterion, Skolithos*; *Netto and Rossetti,* 2003; *Rossetti and Góes,* 2009; *Rossetti et al.,* 2013].

Sedimentary facies of this Pirabas-Barreiras succession suggest a relative sea-level rise during Oligo-Miocene times [*Rossetti et al.,* 2013]. The top of the Barreiras Formation is characterized by a well-developed lateritic horizon, separating these deposits from Quaternary strata [*Rossetti*, 2004]. This regionally extensive horizon has been dated using (U-Th)/He analysis of supergene goethite. Dating of samples from the Paraíba Basin along the eastern margin and from the São Luis-Grajaú Basin and Cametá Sub-Basin along the equatorial margin yield ages of 17.86–0.86 Ma and 16.45–0.97 Ma, respectively [*Rossetti et al.*, 2012a]. Thus both margins were exposed to subaerial erosion and paleosol formation after ~18 Ma [*Rossetti et al.*, 2013]. These observations suggest that the Barreiras Formation had already been subjected to prolonged sub-aerial exposure before the putative Middle Miocene sea-level highstand occurred [*Miller et al.*, 2005; *Rossetti et al.*, 2013].

The Pirabas and Barreiras Formations are disrupted by minor syn- and post-depositional faulting [*Rossetti and Santos Júnior*, 2004; *Nogueira et al.*, 2010; *Bezerra et al.*, 2011; *Rossetti et al.*, 2012a, 2012b, 2013]. This disruption is overprinted by regional variations in outcrop elevation. The deposits occur at elevations of 24–47 m along the equatorial margin, at 65–84 m along coastal portions of the Borborema Province, and at up to 143 m along the eastern margin (Figure 8a) [*Rossetti et al.*, 2013]. This elevation pattern is consistent with offshore residual depth measurements since higher elevation of the Pirabas-Barreiras succession coincides with positive residual depth measurements (Figure 8a) [*Hoggard et al.*, 2017]. We conclude that the distribution of the Pirabas-Barreiras succession is consistent with Cenozoic regional uplift of the Borborema Province.

Regional uplift and denudation is consistent with thermochronologic measurements (Figures 4b and 8b). Modeling of apatite fission track analyses from Precambrian igneous and metamorphic basement of the São Francisco craton immediately south of the Borborema Province suggests that significant cooling events started at 130 Ma along the eastern edge of this craton and at 60–80 Ma within the interior of the craton [*Harman et al.*, 1998]. Subsequent fission track measurements suggest that denudation events occurred at 100–90 Ma and at 20–0 Ma with a minor event at 65–50 Ma [*Morais Neto et al.*, 2009]. These events are consistent with stratigraphic data from the Potiguar Basin. First, a Late Turonian (ca. 89 Ma) subaerial unconformity occurs at the top of the Jandaíra Formation carbonate platform [*Gil*, 1997]. Second, the Miocene denudation event coincides with a transition from carbonate ramp to progradational clastic deposition observed in sedimentary basins along both the eastern (Pernambuco, Paraíba, Sergipe-Alagoas) [*Córdoba et al.*, 2007; *Campos Neto et al.*, 2007] and equatorial (offshore Potiguar, Ceará) [*Condé et al.*, 2007; *Pessoa Neto et al.*, 2007] margins.

Significantly, regional uplift of the Borborema Province coincides with magmatic activity (Figure 8b). There are two obvious groups: the north-south Macau-Queimadas alignment located onshore, and the Fernando de Noronha-Mecejana alignment that comprises the onshore volcanic fields of Mundau and Mecejana, the Rocas Atoll as well as the Fernando de Noronha archipelago itself [*Misuzaki et al.*, 2002; *Knesel et al.*, 2011]. Volcanic necks, plugs, and basaltic flows of the Macau-Queimadas alignment have ages of 93–6.4 Ma. K-Ar whole rock and $^{40}Ar/^{39}Ar$ dates suggest that two phases of magmatism occurred [*Misuzaki et al.*, 2002; *Souza et al.*, 2003, 2013; *Knesel et al.*, 2011]. The first phase coincides with the Cuó volcanic episode that is restricted to the southern portion of the onshore Potiguar Basin with a peak age of ~90 Ma. The second phase coincides with the Macau episode that occurs in the northern Borborema Province, ranging in age from 72 to 6.4 Ma. No obvious age progression is evident along the Macau-Queimadas alignment. However, the Fernando de Noronha to Mecejana alignment youngs eastward from the coastal Mecejana field near Fortaleza with K-Ar ages of 44–26 Ma, to the Fernando de Noronha archipelago with ages of 12–2 Ma [*Misuzaki et al.*, 2002].

These disparate observations can be aggregated to gauge an optimal value of *v*. A systematic sweep through *v*-*m* space is performed, with *m* and *v* varying between 0.35–0.45 and 0.01–1000, respectively. Multiple inversions of the whole drainage inventory are carried out for different parameter combinations to predict a series of different uplift rate histories, which are extracted and averaged for a set of grid nodes close to the center of the Borborema Province (Figures 6, 8a, and 8b). We find that *v* = 10 yields a cumulative uplift history that is broadly consistent with independent observations (Figures 8c and 8d).

In an integrated thermochronologic and geomorphic study of northeast Brazil, *Japsen et al.* [2012] suggested that 3 km of regional subsidence followed by denudation occurred between 100 and 30 Ma. We emphasise that inverse modeling of drainage networks cannot resolve this putative event since regional values of τ_G rarely exceed 30–40 Ma (Figure 4b). Furthermore, drainage networks do not react to subsidence events in an easily recoverable way (existing knickzones are simply buried and may no longer be visible). The inference that the Borborema Province underwent a phase of rapid Neogene uplift does not necessarily preclude the earlier uplift/subsidence excursion proposed by *Japsen et al.* [2012]. We note in passing that the history of vertical movements presented by *Japsen et al.* [2012] is not regarded as being consistent with other regional geomorphic and stratigraphic constraints [*Peulvast and Bétard*, 2015]. Figure 8d has a poorly resolved pre-Neogene tail. If we use $v = 25$, this tail disappears and regional uplift is confined to the last 30 Ma. Unfortunately, uplift histories calculated using $v > 10$ do not accord with independent constraints elsewhere (Figures 9 and 10).
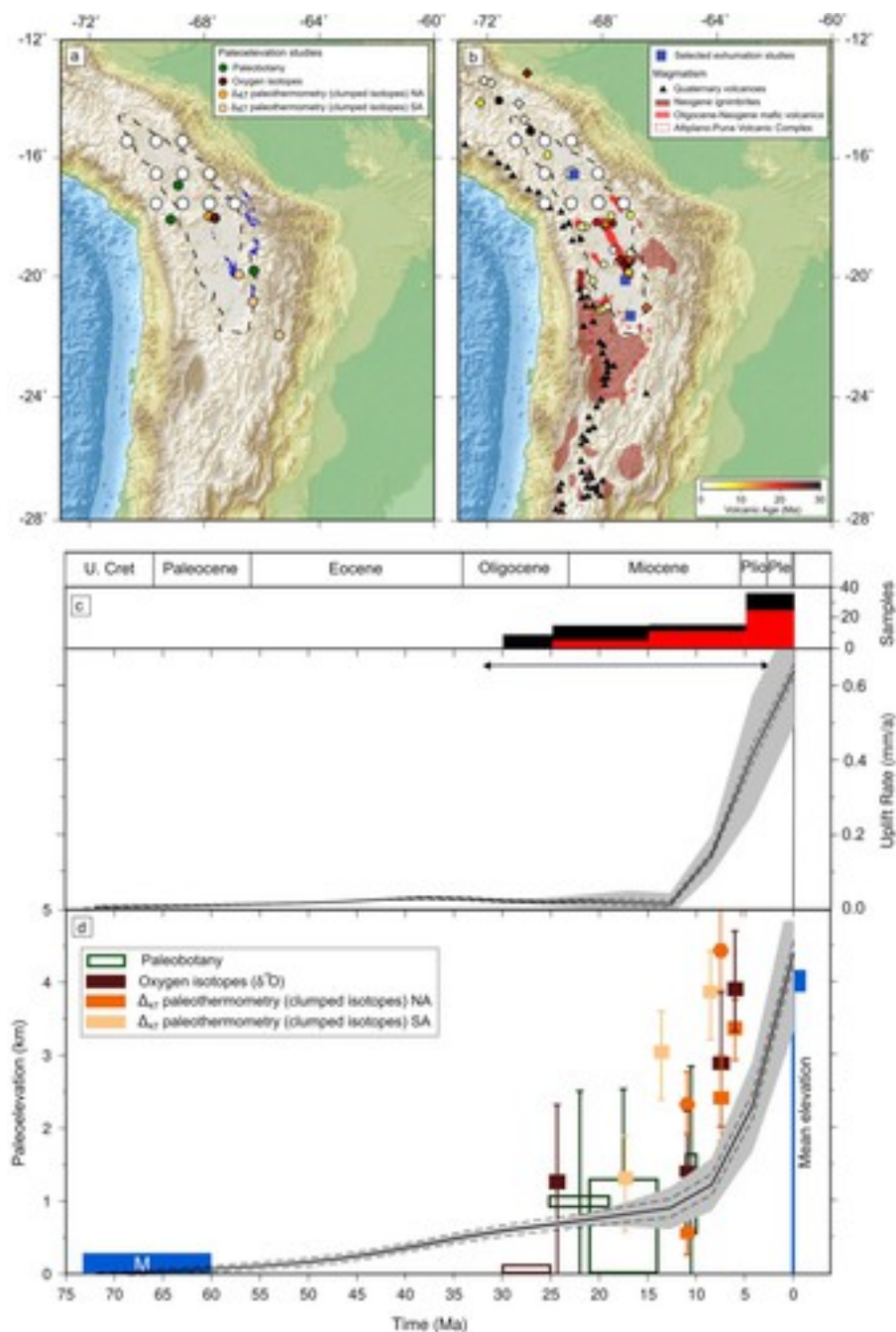
Figure 9
Open in figure viewerPowerPoint

Uplift history of Central Andean Altiplano. (a) Topographic map of western South America. Dashed line = outline of Altiplano sub‐domain [after *Barnes and Ehlers*, 2009]; blue polygons = outliers of shallow marine limestones from Late Cretaceous El Molino Formation [modified from *Horton et al.*, 2001]; colored circles = loci of disparate paleoelevation estimates with key [*Muñoz and Charrier*, 1996; *Gregory‐Wodzicki et al.*, 1998; *Gregory‐Wodzicki*, 2000; *Ghosh et al.*, 2006a; *Quade et al.*, 2007; *Garzione et al.*, 2006, 2014]; NA = northern Altiplano; SA =

southern Altiplano; white circles = loci of nodes whence uplift histories are extracted. (b) Cenozoic magmatism with key (compilation in *Barnes and Ehlers* [2009]). Yellow/orange/red diamonds/circles = dated volcanic rocks (diamonds = ^{40}Ar/^{39}Ar ages from *Davidson and de Silva* [1995], *MacFadden et al.* [1995], and *Carlier et al.* [2005]; circles = K-Ar ages from *Kennan et al.* [1995], *Carlier et al.* [2005], and *Hoke and Lamb* [2007]); blue squares = loci of selected thermochronologic studies [*Barnes and Pelletier*, 2006; *Ege et al.*, 2007; *Barnes et al.*, 2008]; white circles = loci of nodes. (c) Black line with gray band = average predicted uplift rate history with $\pm 1\sigma$ for nodes shown in Figure 9a where dashed lines show changes obtained by covarying *v* and *m* within ranges $5 \leq v \leq 18$ and $0.325 \leq m \leq 0.375$; histogram = magmatism of Central Andean Altiplano (red bars = ^{40}Ar/^{39}Ar ages, black bars = K-Ar ages); horizontal line with arrows = range of exhumation events from thermochronologic studies. (d) Black line with gray band = average predicted cumulative uplift history for nodes shown in Figure 9a; blue squares = original and present-day elevation of sedimentary rocks from shallow marine El Molino Formation [*Sempere et al.*, 1997; *Gregory‑Wodzicki*, 2000; *Barnes and Ehlers*, 2009]; boxes = paleoelevation estimates and uncertainties with key; NA = northern Altiplano; SA = southern Altiplano; hexagons = paleoelevation estimates from clumped isotopic analyses recalculated by *Garzione et al.* [2014] after *Ghosh et al.* [2006a].
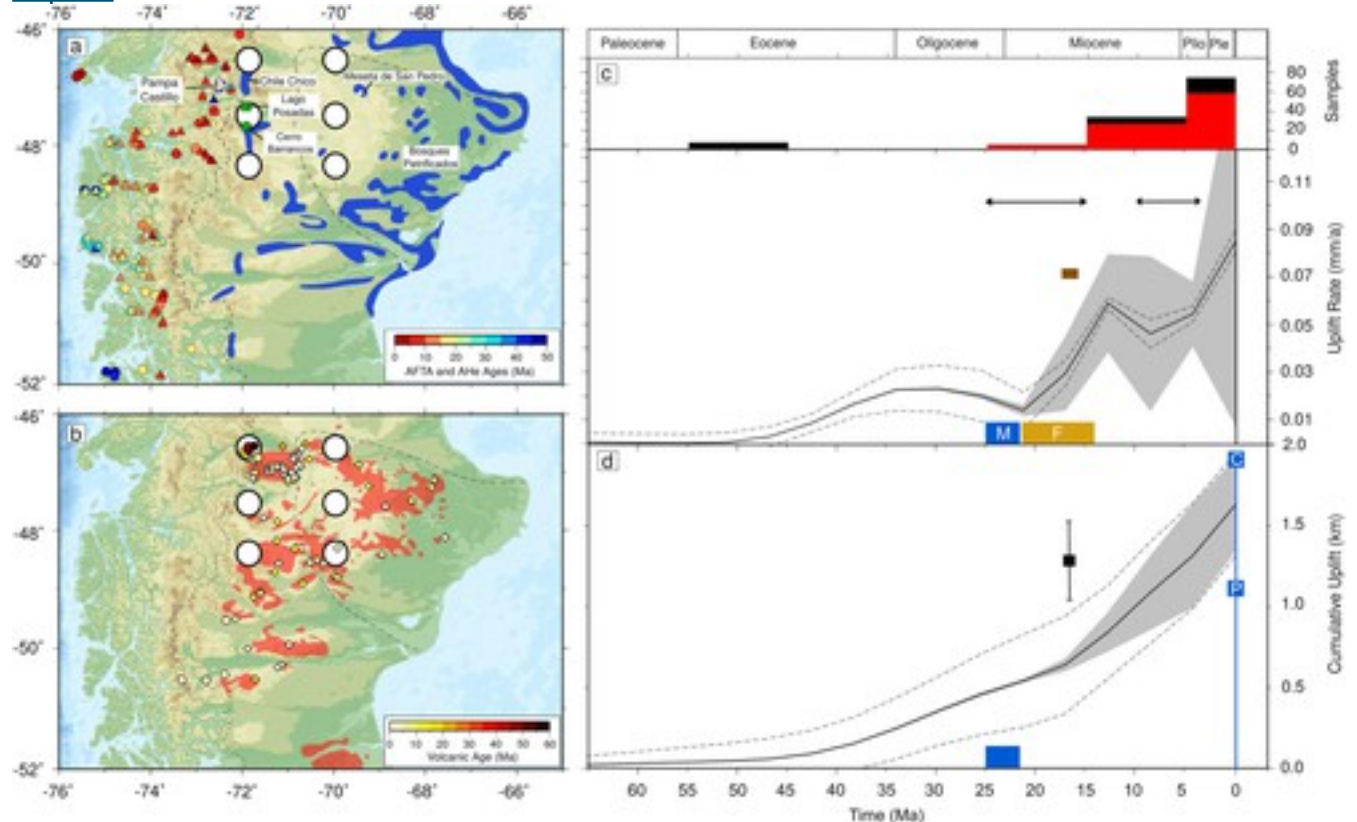
Caption

Figure 10

Uplift history of southern Patagonia. (a) Topographic map with labels indicating locations described in text. Dashed line = outline of Deseado Massif; blue polygons = outliers of Paleocene-Miocene marine deposits [*Suárez et al.*, 2000; *Flynn et al.*, 2002; *Ramos and Ghiglione*, 2008; *Bétard et al.*, 2014]; green box = loci of carbon/oxygen isotopic studies of pedogenetic carbonate nodules [*Blisniuk et al.*, 2005a]; green circle = locus of apatite fission track transect from *Blisniuk et al.* [2005b]; colored circles/triangles = loci of AFT/AHe samples of thermochronologic studies [*Thomson et al.*, 2001, 2010; *Guillaume et al.*, 2013]; white circles = loci of nodes whence uplift rate and cumulative uplift histories are extracted. (b) Cenozoic magmatism. Red polygons = basaltic plateaux [*Ramos and Kay*, 1992; *Gorring et al.*, 1997]; yellow/orange/red diamonds/circles = dated volcanic rocks (diamonds = ^{40}Ar/^{39}Ar ages from *Gorring et al.* [1997], *Ton-That et al.* [1999], *Mejia et al.* [2004], and *Singer et al.* [2004]; circles = K-Ar ages from *Mercer* [1976]; *Charrier et al.* [1979]; and *Mercer and Sutter* [1982]); white circle = location of same node. (c) Black line with gray band = predicted average uplift rate history with $\pm 1\sigma$ for nodes shown in Figure 10a where dashed lines show changes obtained by covarying *v* and *m* within ranges $5 \leq v \leq 18$ and $0.325 \leq m \leq 0.375$; histogram = magmatic samples from southern Patagonian Plateau (red bars = ^{40}Ar/^{39}Ar ages, black bars = K-Ar ages); pair of horizontal lines with arrows = cooling/exhumation events of thermochronologic studies; brown band = onset of increased aridity on leeward side of Patagonian Andes based upon isotopic studies; blue square = youngest marine deposition; yellow rectangle = fluvial deposition [*Flint et al.*, 1994; *Blisniuk et al.*, 2005b]. (d) Black line with gray band = predicted average cumulative uplift history for nodes shown in Figure 10a; blue squares = original and present-day elevation of Late Oligocene marine sedimentary rocks at Chile Chico (C) and Pampa Castillo (P) [*Flynn et al.*, 2002]; black square with error bar = paleoelevation estimate at locus of green box shown in Figure 10a.

5 Regional Geologic Constraints

It is possible to test the continent-wide validity of particular values of *v* and *m* by testing our results against the geologic evolution of more distal regions. Here, we select three regions to test the predicted cumulative uplift history shown in Figure 6. The first region is the Central Andean Altiplano on the opposite side of South America. A large number of detailed thermochronologic and paleoaltimetric studies of this plateau have been carried out. The second region is southernmost Patagonia, where recent studies have suggested that Neogene epeirogenic uplift

has occurred. Finally, we use the predicted history of cumulative uplift to calculate the evolution of fluvial incision for the Amazon catchment. Using this history, we estimate the solid sedimentary flux delivered to the offshore Amazon cone.

5.1 Altiplano Region

Two end-member models of plateau uplift have been proposed [*Barnes and Ehlers*, 2009]. A rapid uplift model suggests that an average elevation of 2.5 km was achieved during Late Miocene times (10–6 Ma) [*Gregory‑Wodzicki*, 2000; *Ghosh et al.*, 2006a; *Garzione et al.*, 2006, 2008, 2014; *Quade et al.*, 2007; *Schildgen et al.*, 2007, 2009, 2010]. A slow model proposes that uplift began in Late Eocene times [e.g., *Allmendinger et al.*, 1997; *Lamb and Hoke*, 1997; *McQuarrie et al.*, 2005; *Hartley et al.*, 2007; *Ehlers and Poulsen*, 2009; *Insel et al.*, 2012]. Here, we use a range of geologic observations to test our independent model of uplift.

In Figure 9, we present a compilation of observations that constrain timing and magnitude of uplift of the Altiplano. Outliers of the El Molino Formation demonstrate that the Altiplano was close to sea level until Early Paleocene times [*Sempere et al.*, 1997; *Lundberg et al.*, 1998]. These shallow marine limestones were deposited between 73 and 60 Ma and crop out across the present-day Altiplano and Eastern Cordillera (Figure 9a). Deposits contain abundant and varied marine fauna that include nannoplankton, foraminifera, dinoflagellates, echinoids, flat-bodied selachians, the operculum of an ammonite, and actinopterygian fish [*Gayet et al.*, 1993; *Okamura and Mamani*, 1994; *Sempere*, 1994]. These deposits now sit at a mean elevation of 4 km [*Sempere et al.*, 1997; *Gregory‑Wodzicki*, 2000; *Barnes and Ehlers*, 2009].

Additional observations suggest that regional uplift occurred within the last 30–35 Ma. First, paleoelevation estimates obtained from paleobotanical and oxygen/clumped isotopic studies imply that the Altiplano remained close to sea level until ∼25 Ma. Nearest-living-relative and leaf physiognomic methods suggest that the Altiplano reached an elevation of 1000 m by 19 Ma, $\leq$ 1320 m by 14 Ma, and 1590–1610 m by 10 Ma [*Muñoz and Charrier*, 1996; *Gregory‑Wodzicki et al.*, 1998; *Gregory‑Wodzicki*, 2000]. Paleoelevation estimates from $\delta^{18}O$ measurements of carbonate paleosols suggest that the Altiplano was low-lying prior to 24.5 Ma, reaching $\leq$2000 m between 25.4 and 11.5 Ma [*Garzione et al.*, 2008]. This uplift event was followed by a rapid rise between 11 and ∼6 Ma when the present-day elevation was reached [*Garzione et al.*, 2006; *Quade et al.*, 2007]. Paleoaltimetric studies based on the degree of clumping between carbon and oxygen isotopes (Δ_{47} paleothermometry) are used to constrain past temperatures of soil formation. This approach can be used to help quantify elevation [*Ghosh et al.*, 2006b; *Quade et al.*, 2013]. Measurements from carbonate paleosoils of the north‑central

Altiplano suggest that the region rose from 600 ± 200 m to 3300 ± 400 m between 10.3 and 6.7 Ma [*Ghosh et al.*, 2006a; *Quade et al.*, 2007]. *Garzione et al.* [2014] carry out Δ_{47} paleothermometry on samples from the southern Altiplano and recalculate the paleoelevations of *Ghosh et al.* [2006a] for the north-central Altiplano. Their results yield higher values for the north-central region and suggest that uplift of the southern Altiplano preceded that of the north-central area by 7 ±4 Ma (Figure 9d).

Paleoaltimetric constraints are controversial and absolute paleoelevation values are uncertain. Oxygen isotopes and clumped isotopes are known to be sensitive to paleoclimatic changes, which can alter values of δ^{18}O precipitation and surface air temperatures [*Barnes and Ehlers*, 2009; *Ehlers and Poulsen*, 2009; *Insel et al.*, 2012]. Nevertheless, Figure 9d shows that, even though individual estimates from different techniques are uncertain, they are broadly consistent with regional uplift of the Altiplano region during the last 25 Ma. Alone, these observations do not discriminate between a slow and steady rise since $\geq$25 Ma and a more rapid rise since 10–6 Ma [*Barnes and Ehlers*, 2009].

Uplift and erosion of the Central Andean Altiplano during Neogene times is supported by thermochronologic studies (Figures 4b and 9d). Exhumation propagated away from the Eastern Cordillera since Late Eocene times and continued until Plio-Pleistocene times [*Barnes and Ehlers*, 2009]. *Ege et al.* [2007] found that exhumation had started in the Eastern Cordillera by ∼40 Ma and spread across the Altiplano at 33–27 Ma, continuing until 11–7 Ma with an apparent exhumation rate of 0.2 mm yr⁻¹. Apatite and zircon fission track analyses by *Barnes et al.* [2008] suggest that initial exhumation of the Eastern Cordillera occurred by 40–35 Ma and that exhumation in the south-central Altiplano started between 30 and 3 Ma and ended at 15–0 Ma. Additional studies within the north-central part of the Altiplano show rapid cooling from 18–2 Ma and increased Late Miocene erosion [*Barnes and Pelletier*, 2006; *McQuarrie et al.*, 2008a].

Magmatic activity provides indirect constraints for the development of the Central Andes and the Altiplano regions [*Barnes and Ehlers*, 2009]. Widespread rhyolitic to mafic back-arc magmatism started at ∼25 Ma throughout a 300 km wide zone within the central Altiplano (Figures 9b and 9c) [*Davidson and de Silva*, 1992, 1995; *Allmendinger et al.*, 1997; *Lamb and Hoke*, 1997; *Carlier et al.*, 2005; *Trumbull et al.*, 2006; *Hoke and Lamb*, 2007; *Kay and Coira*, 2009]. Rare earth elemental compositions of basaltic rocks suggest mantle melting at a depth <90 km. He³/He⁴ ratios have a clear upper mantle affinity [*Hoke and Lamb*, 2007]. Both observations are consistent with thin (∼100 km) lithosphere beneath the Altiplano during Neogene times [*Hoke and Lamb*, 2007].

Finally, deep Late Miocene incision along the margins of the Andean Plateau has occurred, particularly along the western flank [*Barnes and Ehlers*, 2009]. Between 9 and 2 Ma, 1–2.5 km of incision has been identified in the Ocoña‐Cotahuasi canyon on the northwest flank of the plateau using (U-Th)/He apatite thermochronology and $^{40}Ar/^{39}Ar$ dating of incised ignimbrites and perched lava flows [*Schildgen et al.*, 2007; *Thouret et al.*, 2007]. Further south, *Sébrier et al.* [1988] observed downcutting of three dated pediplains, with $\geq$ 400 m of incision between 16 and 11 Ma, 1000 m between 11 and 5 Ma, and 200–1000 m within the last 5 Ma. Similarly, incision of 300–1000 m during the last 8 Ma and >1000 m during the last 10 Ma are interpreted for the central area from river profile analysis, from volcanic stratigraphy, and from fluvial terraces [*Kober et al.*, 2006; *Schlunegger et al.*, 2006; *Hoke and Lamb*, 2007]. There is evidence for youthful incision along the eastern margin of the plateau. For example, *Kennan et al.* [1997] mapped incised paleosurfaces along the central part of the Eastern Cordillera of Bolivia. They noted minor Miocene‐Pliocene down‐cutting followed by increased rates of incision after 3 Ma that generated deep (~1000 m) gorges. Cooling within the last 2–5 Ma was probably caused by recent fluvial incision [*Barnes and Pelletier*, 2006; *McQuarrie et al.*, 2008a].

A smooth cumulative uplift history predicted by calibrated inverse modeling is broadly consistent with these geologic observations (Figures 9c and 9d). The Altiplano region appears to have reached ~600 m of elevation by 25 Ma, although uplift continues to the present-day. Our inverse model predicts slow and steady uplift since 45–40 Ma with a minor uplift event of about 500 m between 25 and 12 Ma and a main uplift event of more than 2 km between 8 and 0 Ma. The first event coincides with initiation of widespread back‐arc magmatism and the second coincides with significant incision of the western flank of the Altiplano. The predicted uplift history also agrees with paleoaltimetric estimates, which indicate that the Altiplano experienced a pulse of rapid uplift during Late Miocene times [*Ghosh et al.*, 2006a; *Garzione et al.*, 2008, 2014].

5.2 Southern Patagonian Andes

Cenozoic regional uplift of the Patagonian Andes occurred on a range of time and length scales [*Ramos and Ghiglione*, 2008; *Guillaume et al.*, 2013]. At present, significant changes in topographic relief occur north and south of the Chile Triple Junction at 46° 30'S [*Ramos and Kay*, 1992; *Thomson et al.*, 2001; *Kay et al.*, 2004; *Haschke et al.*, 2006; *Guillaume et al.*, 2009, 2013]. An average elevation of 2300 m occurs to the north of 46° 30'S. In the southern Patagonian Andes, there is a dramatic increase in relief with peaks as high as 4070 m [*Thomson et al.*, 2001; *Ramos and Ghiglione*, 2008]. This difference could be a consequence of subduction of part of the Chile Ridge during late Cenozoic (∼14 Ma) times west of Tierra del Fuego [*Cande*

and Leslie, 1986]. It is postulated that this event led to the generation and progressive enlargement of an asthenospheric window [*Breitsprecher and Thorkelson,* 2009]. Development and migration of this slab window could have triggered regional dynamic uplift that affected the Patagonian Cordillera and the Southern Patagonian Plateau and caused modification of drainage networks and differential uplift of Quaternary marine terraces along the South Atlantic margin [*Guillaume et al.,* 2009, 2013; *Schellmann and Radtke,* 2010; *Pedoja et al.,* 2011a]. Figure 10 summarizes independent observations of uplift for the Southern Patagonian Andes. Figures 10a and 10b show the spatial distribution of marine sedimentary rocks, thermochronologic observations, and magmatism. Figures 10c and 10d compare these observations with our predictions.

The most straightforward evidence for Cenozoic uplift of the Southern Patagonian Andes is the distribution of Oligo-Miocene shallow marine sedimentary rocks that represent the final manifestation of the Patagonian Seaway, a widespread marine transgression that extended across most of southern Patagonia [*Malumián and Ramos,* 1984; *Flint et al.,* 1994; *Suárez et al.,* 2000; *Flynn et al.,* 2002; *de la Cruz and Suárez,* 2006]. Outliers of near-shore marine sandstones, conglomerates, and shales crop out in several regions. They are referred to as the Guadal Formation in Chile [*Suárez et al.,* 2000; *de la Cruz and Suárez,* 2006], the Centinela Formation in Argentina [*Lagabrielle et al.,* 2007; *Parras et al.,* 2008], and the Chenque and Monte León Formations along the South Atlantic margin [*Malumián,* 1999; *Parras et al.,* 2008]. Today, outcrops of the Guadal Formation are found at elevations of 1900–1950 m southwest of Chile Chico and at an elevation of 1100 m at Pampa Castillo [*Flynn et al.,* 2002] (Figures 10a and 10d). Marine fossils include abundant macroinvertebrate fauna (e.g., oysters, brachiopods, bryozoa, echinoids) [*Frassinetti and Covacevich,* 1999]. This series is conformably overlain by fluvial deposits of the Santa Cruz Formation and its lateral equivalents (e.g., Río Zeballos Group) [*Ramos,* 1989; *Suárez et al.,* 2000; *de la Cruz and Suárez,* 2006]. Deposits comprise interbedded sandstones and silts with conglomerate lenses that were deposited in a high-energy fluvial environment [*Ramos,* 1989; *de la Cruz and Suárez,* 2006]. Radiometric dates from intercalated tuffaceous deposit along the foothills of the Cordillera yield 22–14 Ma [*Blisniuk et al.,* 2005a]. These sedimentary facies suggest that regional uplift had already triggered regression of the Patagonian seaway and establishment of continental conditions [*Ramos,* 1989; *Ramos and Ghiglione,* 2008]. In a study of a section from the Santa Cruz Formation at Lago Posadas (eastern foothills of the Cordillera; Figure 10a), *Blisniuk et al.* [2005a] identified an increase in mean depositional rate between 18 ± 0.3 and 16.7 ±0.6 Ma from 0.012 ±0.002 mm yr^{-1} to 0.114 ±0.025 mm yr^{-1}. This increase coincides with a switch to more arid conditions on the lee side of the eastern foothills that is supported by both paleontologic data and stable carbon isotopic

analysis [*Blisniuk et al.*, 2005a]. Comparison of mammalian taxa from the Santa Cruz Formation and younger assemblages suggests a change from subtropical humid climate in woodlands and grasslands to a cooler and more arid climate [*Pascual*, 1990; *Flynn and Swisher*, 1995; *Flynn et al.*, 2002]. Results from carbon isotope analysis of pedogenic carbonate nodules from the Santa Cruz Formation show an increase in $\delta^{13}C$ values at ∼16.5 Ma that is interpreted as the effect of low water availability [*Blisniuk et al.*, 2005a]. In the same study, a decrease in $\delta^{18}O$ values at ∼16.5 Ma is interpreted as a consequence of ∼1km of surface uplift.

Thermal modeling carried out by *Thomson et al.* [2001] along the western side of the Cordillera between 44°S and 51°S reveals an increase in cooling and denudation at 30–23 Ma, followed by another phase of denudation between 12 and 8 Ma adjacent to the present-day topographic divide. Assuming that the average geothermal gradient during Miocene times was similar to that of the present day (i.e., $30\pm10°C/km$), 4–9 km of denudation is inferred to have occurred. Fission track samples acquired along a 2000 m elevation profile from the Cerro Barrancos pluton indicate that accelerated cooling started at ∼17 Ma, followed by a reheating event at 10–6 Ma with accelerated cooling since 4 Ma (Figures 4b and 10a) [*Haschke et al.*, 2006]. *Guillaume et al.* [2013] carried out (U-Th)/He apatite thermochronology along three transects from the leeward eastern side of the Patagonian Cordillera. Two of these transects are included within the area discussed here, one at 46.5°S and another one at 47.57°S which corresponds to the Cerro Barrancos Pluton. Slower cooling occurred between 25 and 15 Ma (corresponding to a denudation of 70 m Ma⁻¹), followed by a reheating phase at ∼15 Ma. Later, slow cooling started at 10 Ma for the transect at Cerro Barrancos and at 7 Ma for the transect at 46.5°S. A significant pulse of rapid cooling occurred between 6 and 3 Ma, which implies a denudation event of about 1.3 km with a steeper geothermal gradient of 60°C/km. Thermal modeling of the Cerro Barrancos samples carried out by *Guillaume et al.* [2013] shows a difference of 5 Ma in onset of the reheating phase with respect to the thermal histories of *Haschke et al.* [2006]. Reheating and subsequent uplift are interpreted as a consequence of mantle flow related to slab window opening and migration [*Guillaume et al.*, 2013]. Finally, the low-temperature thermochronology of *Thomson et al.* [2010] between 38°S and 56°S indicates accelerated denudation at 7–5 Ma north of 49°S and younger than 10 Ma further south.

The events identified by *Haschke et al.* [2006] and *Guillaume et al.* [2013] coincide with a pause in arc volcanism and significant eruption of plateau basalts across the eastern foothills between 46.3°S and ∼50°S [*Ramos and Kay*, 1992; *Gorring et al.*, 1997]. These Late Cenozoic plateau lavas are divided into two sequences that relate to different stages of ridge subduction and slab window development. There is a Late Miocene to Early Pliocene sequence of voluminous,

mainly tholeiitic, plateau basalts that form large elevated mesas. A Late Miocene to Plio-Pleistocene alkalic sequence of less voluminous extrusions then occurred, characterized by minor cones, lava flows, pyroclastic debris, and low elevation mesas. Trace element and isotopic compositions indicate high percentages of melting from a mantle source of oceanic island basalt (OIB) type, with higher melt percentages for main plateau basalts compared to postplateau lavas. *Ramos and Kay* [1992] suggest that Neogene plateau lavas form as a consequence of slab window opening and migration. *Gorring et al.* [1997] and *Gorring and Kay* [2001] suggest that main plateau lavas are the consequence of interaction between upwelling asthenosphere, which flows around the trailing edge of the subducting Nazca slab, and continental lithosphere.

Additional observations suggest that regional uplift has also influenced the whole eastern foreland of the Patagonian Andes between 46°S and 50°S. Here, the Deseado Massif, a 1335 m high platform characterized by a low relief tableland, occurs (Figures 10a and 10b). In their morphostratigraphic analysis, *Bétard et al.* [2014] quantify long-term uplift and denudation since Mesozoic times. Relics of Paleogene-Neogene shallow marine sedimentary rocks crop out across this massif [*del Río,* 2002]. In the Bosques Petrificados area in the center of the massif, Oligo-Miocene marine sedimentary rocks of the Monte León Formation occur at 600 m elevation. These deposits are part of the Patagonian transgression and are equivalent to the Guadal and Centinela Formations observed in the eastern Andean foothills. Maximum Neogene uplift is recorded in the northern part of the massif, where the Monte León Formation crops out at 1000 m elevation below a basaltic surface known as the Meseta de San Pedro (Figure 10a). The differential elevation of these two remnants implies southward tilting of the Deseado Massif [*Bétard et al.*, 2014]. This tilting has also been observed by *Guillaume et al.* [2009] using the distribution of post-Middle Miocene fluvial terraces. Uplift of marine terraces along eastern Patagonia demonstrates that regional uplift continued into Quaternary times [*Pedoja et al.*, 2011a]. Late Miocene plateau basalts also cover a significant part of the Deseado Massif. Here, *Bétard et al.* [2014] estimated the amount of denudation using topographic inversion of lava flows, which originally filled paleodepressions and paleovalleys that now form mesas or buttes. Maximum post-Miocene denudation is observed for the basalts of the Meseta de San Pedro, with values of ~800 m since 5 Ma. East of Bosques Petrificados, 15 Ma old basaltic mesas occur at ~750 m. Additional evidence for Cenozoic uplift of the Deseado Massif is manifest by uplifted remnants of the Gondwana paleosurface, an ancient planation surface of possible Late Jurassic to Early Cretaceous age that is widely recognized throughout South America [*Rabassa et al.*, 2010]. In the Deseado Massif, *Bétard et al.* [2014] show that this regional paleosurface bevels Middle-Late Jurassic volcanic rocks of the Bahía Laura Group and is unconformably overlain by the Bajo Grande and Baqueró Formations of Cretaceous age. This

paleosurface is partly incised and laterite formation is identified in places [*Aguilera et al.*, 2012]. Eastward tilting remnants of this surface are found at ~800 m in the western highlands of the Massif. The same tilting surface can be identified at lower elevations in the eastern plains.

We compare these observations to our average predicted cumulative uplift history (Figures 10c and 10d). The region was at, or near, sea level in Paleogene times. A minor phase of regional uplift produced an elevation of ~500 m by 20 Ma. However, geologic observations suggest that the eastern foreland was submarine in Oligo-Miocene times. We attribute this discrepancy to the conservative degree of spatial smoothing used by the inverse algorithm. Thermochronologic observations from the western side of the present-day Cordillera confirm the onset of rapid exhumation by 30 Ma [*Thomson et al.*, 2001]. Analysis of Miocene marine deposits of the Guadal and Centinela Formations that crop out along the eastern foothills of the Cordillera, and of coeval deposits along the Pacific margin, show that fauna are different to each other, suggesting that the Patagonian transgression did not reach the Pacific margin [*Frassinetti and Covacevich.*, 1999; *Flynn et al.*, 2002]. Our smooth uplift history reflects this pre-Cenozoic uplift event affecting the Cordillera and western foothills. Significant uplift appears to have started at ~20 Ma, coincident with the transition from marine to fluvial deposition [*Ramos and Ghiglione*, 2008], and with onset of increased denudation [*Haschke et al.*, 2006; *Guillaume et al.*, 2013]. Peak uplift rates of ~0.06 mm yr^{-1} coincide with the heating event inferred by *Guillaume et al.* [2013] and with eruption of plateau basalts. A smaller uplift event at 5 Ma coincides with the onset of more rapid exhumation [*Thomson et al.*, 2001; *Haschke et al.*, 2006; *Guillaume et al.*, 2013] and with the eruption of postplateau sequences [*Gorring et al.*, 1997]. Paleoelevation estimates for the Southern Patagonian Andes are limited to those of *Blisniuk et al.* [2005a], who place the region at ~1000 m by 16.5 Ma using δ^{18}O values. Our model predicts a cumulative uplift of ~700 m at 16 Ma. A better constraint is the present-day elevation of marine deposits from the Guadal and Centinela Formations, which agrees with our prediction (Figure 10d). Despite this agreement, predicted uplift rate histories for the last ~10 Ma show significant spatial variability (Figure 10c). We attribute this variability to small differences in the shapes of river profiles that may imply the presence of short-scale tectonic features such as faulting.

5.3 Amazon Catchment and Fan

The Amazonian landscape and drainage are affected by regional uplift of the Andes. Development of the Amazon Fan is a direct consequence of this uplift [*Hoorn et al.*, 2010; *Gregory-Wodzicki*, 2000; *Figueiredo et al.*, 2009; *Latrubesse et al.*, 2010]. A significant and independent way of gauging the quality of our regional uplift patterns is to

analyze the sedimentary flux history of the Amazon river and its tributaries. Here, we compare predicted sedimentary flux to facies distribution and measured rates of deposition from the Foz do Amazonas.

Before Late Miocene times, present-day Amazonia appears to have been part of a larger catchment that probably included the present-day Magdalena and Orinoco drainage basins [*Hoorn et al.*, 2010]. Sedimentologic and paleontologic studies of the Amazonian foreland basin system show that the western and northwestern parts of this vast region were occupied during Paleogene times by extensive lowlands characterized by fluvial deposition with occasional marginal marine influence [*Hoorn et al.*, 2010; *Roddaz et al.*, 2010]. By Early Miocene times, lithologic provenance, sedimentary sequences, and paleotransport directions suggest that western Amazonia, a region occupied today by the low-lying sub-Andean foreland basins and by the intracratonic Solimões basin, was dominated by a northwesterly directed fluvial system with major clastic input from both the Guyana Shield and the Amazon craton [*Hoorn et al.*, 2010]. At the locus of the present-day Amazon Fan, the continental shelf was a carbonate platform that was periodically interrupted by minor siliciclastic deposition [*Figueiredo et al.*, 2009]. Between Early and Middle Miocene times, regional uplift of the Northern and Central Andes and coeval subsidence caused this fluvial pattern to evolve into a mega-wetland system of shallow lakes and swamps known as the Pebas System. This evolution is recorded by the Solimões and Pebas Formations [*Figueiredo et al.*, 2009; *Hoorn et al.*, 2010]. Between 23 and 16 Ma, lacustrine conditions alternated with fluvial episodes. Between 16 and 12 Ma, the wetlands expanded eastward to reach their maximum extent. Deposits mainly comprise clays, lignites, and thin immature sandstones with sedimentary structures typical of a low energy, tidally influenced environment. They are also characterized by abundant, well-preserved aquatic fauna (e.g., freshwater mollusks, ostracods, fish together with reptiles such as caimans, gharials, and turtles) [*Hoorn et al.*, 2010]. Terrestrial vegetation was dominated by rainforest taxa and swamps were populated by palm and grass meadows [*Hoorn et al.*, 2010]. Marine incursions have been proposed, based upon marine taxa and upon the presence of benthic foraminifera, barnacles, dinoflagellates, and marine mollusks within thin beds intercalated by fluvial deposits [*Lovejoy et al.*, 2006; *Wesselingh et al.*, 2006]. Further evidence for periodic brackish environments comprises mangrove pollen and marine ichnofossils such as *Glossifungites* [*Hovikoski et al.*, 2007].

In eastern Amazonia, a nascent Amazon river dissected the hinterland, transporting minor volumes of clastic sediments onto the continental margin and episodically interrupting carbonate production. Provenance studies from two wells drilled into the Foz do Amazonas basin and into

the uppermost Amazon Fan suggest that the Guyanan craton was the main source for this ancestral Amazon river [*Figueiredo et al.*, 2009]. Stratigraphic records from the Solimões [*Ribeiro et al.*, 2007] and Amazon [*Cunha et al.*, 2007] intracratonic basins imply that, by this time, western and eastern Amazonia were separated by the Purus arch. At 12 Ma, deep canyon incision and erosion began to affect the uplifting Northern and Central Andes [*Schildgen et al.*, 2007, 2009, 2010; *Thouret et al.*, 2007; *Restrepo-Moreno et al.*, 2009]. The mega-wetland of western Amazonia gradually evolved into a fluviodeltaic system known as the Acre system. Channel deposits are intercalated with pedogenic or root-bearing horizons. Double mud drapes, reactivation surfaces within heterolithic cross-strata, sigmoidal ripples, cyclic rhythmites, and ichnofossil assemblages (e.g., *Gyrolithes, Skolithos, Ophiomorpha*) suggest that these sediments were deposited in fluvial, deltaic, and estuarine channel complexes with tidal influence [*Hoorn et al.*, 2010]. However, the existence of marine influence within these deposits is debated. Studies suggest that Late Miocene deposits of western Amazonia are continental. This assertion is based on vertebrate fossils and facies analysis. *Latrubesse et al.* [2007, 2010] and *Gross et al.* [2011] argue that evidence for tidal influence is mainly based on diagnostic sedimentary structures. A connection was established between east and west Amazonia by breaching of the Purus arch. Between 11.8 and 11.3 Ma, Andean sediments started to reach the Atlantic coastline along an established Amazon river. This event is recorded as an unconformity marking onset of the Amazon Fan [*Figueiredo et al.*, 2009]. Provenance studies of Late Miocene deposits from a well drilled into the Amazonas basin shelf identify Andean-sourced sediments. *Figueiredo et al.* [2009] divided development of the Amazon Fan in three phases. In the onset phase (11.8–6.8 Ma), the Amazon river was not entrenched and deposition was weak with a mean rate of 0.05 m ka^{-1}. In the middle phase (6.8–2.4 Ma), the river was fully entrenched and sedimentation rate significantly increased to a mean rate of 0.3 m ka^{-1}, suggesting that the growing Andes had become the main source. This phase also coincides with the disappearance of wetlands in western Amazonia at ~7 Ma. After 2.4 Ma, the Amazon river acquired its present-day configuration and mean sedimentation rates reached 1.22 m ka^{-1} with a peak of 11.16 m ka^{-1}. Provenance studies are consistent with a pulse of craton-sourced sedimentation during Early Pliocene times (i.e., 4.2 Ma) that could be linked to a pulse of uplift affecting the Guyana shield further north.

In Figure 11, we compare flux estimates calculated by *MacGregor* [2012] from his detailed analysis of cross sections and seismic profiles with our flux history that is calculated by reconstructing river profiles within the catchment at different times. The difference between successive profiles is a measure of the area of sediment eroded as a function of time. By integrating this area over successive profiles for each time step, the amount of sedimentary flux

for a given catchment is determined [*Paul et al.*, 2014; *Stephenson et al.*, 2014]. We use this approach to gauge sedimentary flux for 116 river profiles from the catchment. Our predicted sedimentary flux history shows increasing efflux through time with low values during pre-Miocene times and significantly higher values during the last ~15 Ma. Results are consistent with the observed sedimentary history [*MacGregor*, 2012] (Figures 11b–11g). At 36 Ma, when the continental shelf comprised a carbonate platform with episodic clastic deposition, we predict little incision within the drainage basin. Minor amounts of incision affected the Guyana Shield and the Amazon craton to the north and south of the catchment, respectively. At 21 Ma, when intensified uplift initiated in the Northern and Central Andes, a wetland occupied western Amazonia and the ancestral Amazon river developed in eastern Amazonia. Calculated incision is greater but is focused in cratonic regions that surround the Amazon basin. At 11 Ma, significant uplift of the Northern and Central Andes is predicted by our inverse model (Figure 6). At that time, incision became widespread, consistent with the arrival of Andean-sourced sediments at the nascent Amazon Fan [*Figueiredo et al.*, 2009]. By Pleistocene times, incision was affecting the entire Northern and Central Andes. Thus, our calculated incision and sedimentary flux histories for the Amazon basin are consistent with independent geological observations of deposition in the Foz do Amazonas, with development of the Amazon Fan, and with evidence that Andean uplift had a dominant control on the evolution and distribution of drainage patterns.
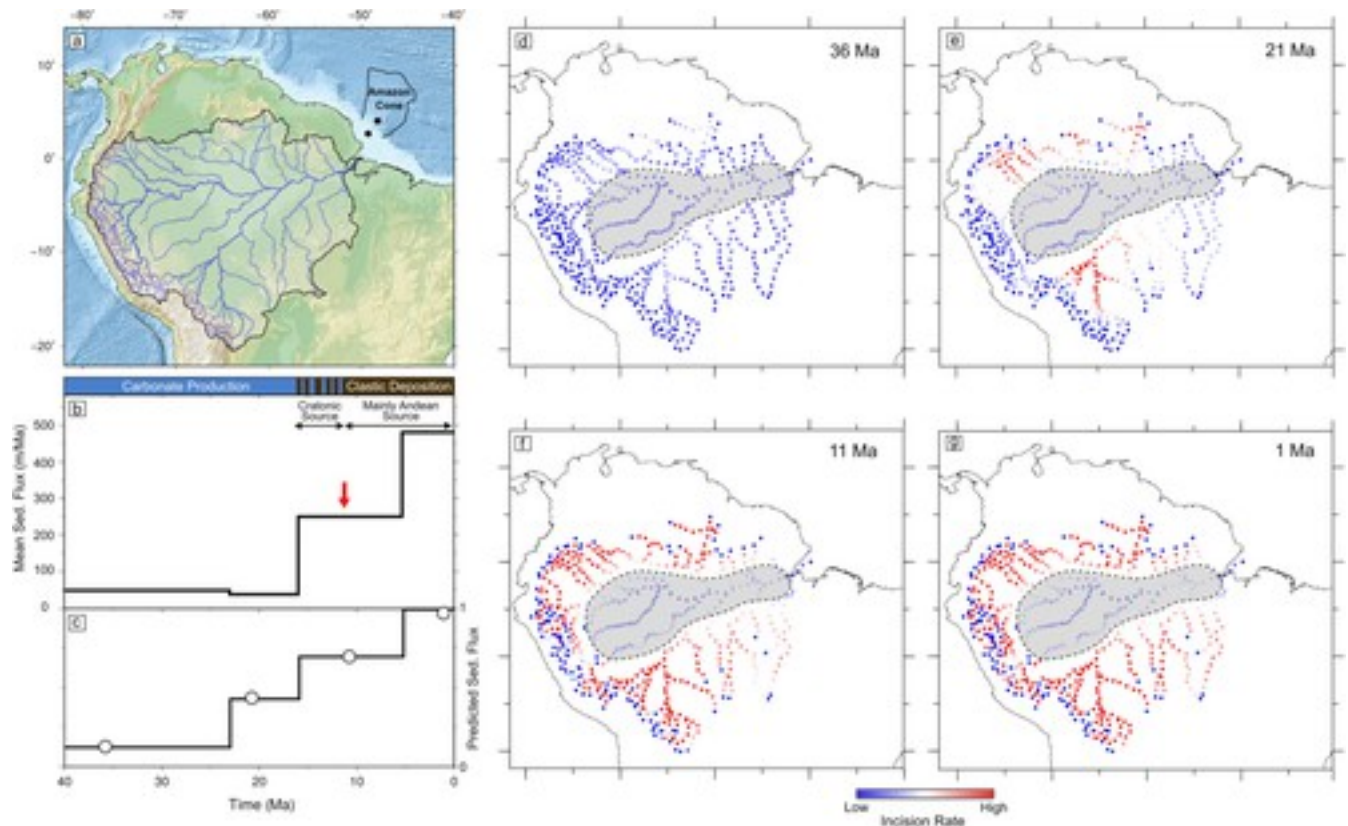
Figure 11
(a) Map of Amazon catchment showing recovered drainage pattern and locus of Amazon cone (i.e., Foz do Amazonas). Blue lines = 116 river profiles used to calculate solid sedimentary flux at Amazon cone; black circles = loci of wells described by *Figueiredo et al*. [2009]. (b) Observed solid sedimentary flux history of Amazon cone estimated using seismic reflection profiles calibrated with well-log information [*MacGregor,* 2012]. Color bar = summary of depositional environment (blue = carbonate platform; blue/brown dashes = carbonate platform periodically disrupted by siliciclastic deposition; brown = siliciclastic deposition); red arrow = age of unconformity recognized in wells; black arrows = age of source regions for Amazon cone sediments [*Figueiredo et al*., 2009]. (c) Normalized and binned flux calculated from uplift history shown in Figure 6. White circles = predicted flux at times shown in Figures 11d–11g. (d)–(g) Reconstructed distribution of incisional events throughout Amazon catchment since 36 Ma (note absence of incision adjacent to Andean Cordillera prior to 11 Ma). Gray polygon = swampy region of low relief with little evidence of incisive events over last 36 Ma.

Caption
Evolution of the Amazonian basin suggests that some drainage reorganization occurred in Middle Miocene times [*Roddaz et al*., 2010; *Hoorn et al*., 2010]. In Paleogene times, the present-day Amazon basin was characterized by low relief topography apart from the Guyana and Amazon cratons, which formed the catchment areas of the easterly flowing proto-Amazon system (Figures 6 and 11). When the Andean cordillera underwent rapid uplift in Miocene times, headwaters of what became the present-day drainage basin were incised, triggering disappearance of the western wetland and establishment of the configuration of the modern Amazon river. It is important to emphasise that uplift signals probably did not advect upstream from the river mouth. Instead, it is more likely that these signals were inserted much closer to the Andean cordillera. A significant consequence of this insertion is that inverse modeling is, in this case, largely unaffected by putative downstream drainage reorganizations.

Previous studies focused on predicting the evolution of the Amazon basin and development of the Amazon cone. *Shephard et al*. [2010] suggest that changes in dynamic topography play a crucial role in evolution of the Amazon basin. Results from their coupled model of mantle convection and plate kinematics suggest that dynamic subsidence of northwest South America at 40–30 Ma caused the formation of the Amazonian mega-wetland. Continuous movement of the South American plate over subducting slabs coupled with subsidence of the eastern Amazonian sedimentary basins would have caused rebound of the mega-wetland area after 30 Ma. Our regional uplift model predicts uplift of northernmost South America at 40–30 Ma, in

disagreement with the pattern of subsidence predicted by *Shephard et al.* [2010] who also predict post-40 Ma subsidence of central and eastern South America. In contrast, we show how regional uplift of northeast Brazil is significant at this time (Figures 6 and 8). *Eakin et al.* [2014] and *Dávila and Lithgow-Bertelloni* [2015] attribute dynamic topography to the Peruvian flat slab. They suggest that transition from normal to flat subduction in Mid-Late Miocene times yielded significant dynamic uplift across the Andes (directly above the flat slab) and relative dynamic subsidence away from the trench that only affects the distal Andean foreland and western Amazonia.

Sacek [2014] advocates a different mechanism for the development of the Amazonian system based upon a three-dimensional numerical model that couples surface processes, flexural isostasy and crustal thickening. This model implies that evolution of the Amazon drainage system was controlled by erosion and redistribution of material, triggered by Andean uplift. The timing of establishment of the modern Amazon river depends on efficiency of the sediment transport and uplift rate of the Andes, which is kept constant in both space and time. This model is able to reproduce the timing of Amazon river development and agrees with estimates of subsidence within the foreland basins, but it fails to predict the evolution of the mega-wetland system.

6 Discussion

6.1 Regional Comparisons

The cumulative uplift history of South America was calculated from continent-wide drainage networks using erosional parameters that were calibrated using the Cenozoic evolution of the Borborema Province on the eastern seaboard. We have tested the validity of this cumulative uplift history by comparing observed and calculated uplift histories for the Altiplano and Patagonian regions. Separately, we exploited the calculated uplift history to construct an incisional history of the Amazon catchment, whence we predict offshore sedimentary flux.

We suggest that uplift initiated in Eocene times within the northern Andes (Figure 6). The bulk of the Andean cordillera appears to have developed during Miocene times. For example, Figure 4b shows a compilation of thermochronologic data across the continent which suggests that most exhumation-related cooling along the Andes occurred within the last 60 Ma. In the Venezuelan Andes, exhumation is tracked back to Oligocene times for the northeastern and southeastern regions of the Venezuelan Andes, whereas the central areas are characterized by Early Miocene, Late Miocene and even early Pliocene events [*Bermúdez et al.*, 2010, 2011]. Late Miocene uplift

in particular is consistent with increased sedimentary flux into the surrounding Maracaibo and Barinas foreland basins [*Bermúdez et al.*, 2011]. Erosional events triggered by uplift are recorded in northernmost Colombia (Sierra Nevada de Santa Marta Massif) during Paleocene (65–58 Ma), Eocene (50–40 Ma), and Oligo-Miocene (30–16 Ma) times [*Villagómez et al.*, 2011]. Further south within the eastern Colombian Andes, thermochronologic studies suggest that cooling started in Late Eocene-Oligocene times and continued until Pliocene times [e.g., *Parra et al.*, 2009]. Pliocene-Holocene uplift of the eastern Colombian Andes is also supported by paleobotanic observations, which suggest that elevations were less than 40% of their modern values between Early/Middle Miocene and Pliocene times. Present-day elevation was only gained at 2.7 ±0.6 Ma [*Gregory-Wodzicki*, 2000]. Additional constraints comprise elevated Late Cretaceous marine deposits, which show that this region was uplifted after that time.

Neogene uplift is recorded in the Ecuadorian Andes by the existence of a relict planation surface that developed at low elevations during Early Pliocene times. It now sits at 3000–3500 m [*Coltorti and Ollier*, 2000]. Thermal modeling of apatite (U-Th)/He data by *Michalak et al.* [2016] also documents Cenozoic regional exhumation within the northern Peruvian Andes. Their thermal histories suggest that slow cooling occurs throughout Paleogene times, followed by rapid increase in cooling rates in Mid-Miocene times (between 14 and 10 Ma; Figure 4). Within northern Peru, three erosional surfaces formed at sea level and have been subsequently elevated and incised during Miocene-Pliocene times [*Michalak et al.*, 2016, and references therein]. Neogene uplift occurs in the Chilean Andes, where *Farías et al.* [2008] describe evidence for post-Miocene regional uplift between 33°S and 35°S (Figure 1a). Here, uplifted shallow marine sedimentary rocks, that are 10.9–4.4 Ma old, are found along the coastline. They are overlain by a lahar deposit with an $^{40}Ar/^{39}Ar$ age of 2.7 ±0.3 Ma. This chronology suggests that uplift occurred after 4.4 Ma but before 2.7 Ma. Emergent Pleistocene marine terraces imply that ~400 m of subsequent uplift took place. Youthful regional uplift of the Chilean Andes is inferred from the existence of elevated peneplains at 1000–3000 m that are incised by kilometer-scale canyons.

Our calculated uplift history predicts regional Cenozoic uplift of the cratonic interior (Figure 1b). Figure 4b shows that this region has diverse thermochronologic ages. Cretaceous cooling of the Brazilian margin is recorded by apatite and zircon fission track modeling [*Harman et al.*, 1998; *Turner et al.*, 2008; *Cogné et al.*, 2011, 2012; *Oliveira et al.*, 2016]. This cooling event is usually interpreted as a manifestation of the start of continental break-up. However, this margin is also characterized by more youthful (i.e., Cenozoic) exhumation.

Jelinek et al. [2014] carried out a thermochronologic study of the Brazilian margin between 8°S and 21°S in which they identified acceleration of cooling in Neogene times. *Gallagher et al.*

[1994] report apatite fission track ages of 60–90 Ma with 3 km of denudation along the coastal plains between 20°S and 30°S (Figures 1a and 4b). *Hackspacher and Ribeiro* [2004] identify an increase of exhumation at ~65 Ma within the Mantiqueira Mountain Range, the Serra do Mar and several plateaux north of São Paulo (Figures 1a and 4b). In the same region, *Franco-Magalhaes et al.* [2010, 2014] and *Cogné et al.* [2012] identify Eocene and post-Miocene cooling events. In southern Brazil, 1–2.5 km of denudation has occurred since ~58 Ma, much of it within the last 15 Ma [*Oliveira et al.*, 2016]. These thermochronologic studies are consistent with a range of evidence for Neogene uplift and with offshore sedimentary flux [e.g., *Cogné et al.*, 2012]. Our results predict that uplift of the Atlantic Shield commenced at ~30 Ma, which is in broad agreement.

Finally, our calculated history reproduces Cenozoic uplift of the Guyana Shield (Figure 6). This cratonic region is characterized by mean low elevations interrupted by table mountains with altitudes of 2 km. Geomorphic studies of the Guyana Shield document five stepped planation surfaces separated by steep escarpments. These surfaces can be correlated across the shield and have different names in different parts of the shield [*McConnell*, 1968; *Briceño and Schubert*, 1990]. Their origin is poorly understood but their morphology and increasing youthfulness with decrease in elevation suggest that they are generated by episodic epeirogenic uplift [*Briceño and Schubert*, 1990]. In the absence of absolute dating, tentative ages have been assigned based on structural and stratigraphic relations. The highest (>1 km) surfaces are probably of Mesozoic age. Lower surfaces may have developed during Late Cretaceous and Paleocene times (525–750 m), Oligocene to Miocene times (200–450 m), Plio-Pleistocene times (80–150 m), and Holocene times (0–50 m) [*Briceño and Schubert*, 1990]. Paleomagnetic dating of overlying ferrigenous and bauxitic duricrusts from French Guyana and Suriname suggest that Paleogene and Late Miocene laterization events are consistent with the inferred age [*Théveniaut and Freyssinet*, 2002].

6.2 Geodynamic Implications

Many, but not all, numerical models of global dynamic topography are characterized by $O(10^4)$ km wavelengths. Many of these models predict that South America has been located over a substantial convective downwelling since Cretaceous times (see review of *Flament et al.* [2013]). However, a database of dynamic topographic measurements assembled by *Hoggard et al.* [2016] shows that observed dynamic topography mostly occurs on much shorter, $O(10^3)$ km, wavelengths. Regional dynamic topographic models generally focus on the influence of the subducting Nazca slab [*Dávila and Lithgow-Bertelloni*, 2013]. *Flament et al.* [2015] use a time-dependent global model to predict the evolution of post-Miocene topography. They argue that

evolution of the Amazon catchment may be affected by large-scale mantle flow. They predict ∼ 580 m of cumulative Neogene uplift at rates of 53 m Ma⁻¹ for the Sierras Pampeanas region. After 13 Ma, uplift rates of 18 m Ma⁻¹ are predicted at 46.6°S within Patagonia. In both cases, dynamic uplift is attributed to onset of flat slab subduction. Our inverse model predicts that ∼1600 m of Neogene uplift occurred in the Sierras Pampeanas region during that time. The predicted uplift rate for Patagonia is ∼90 m Ma⁻¹ at ∼10 Ma. *Flament et al*. [2015] also predict an eastward-migrating wave of dynamic uplift between 65°W and 70°W from 20 to 0 Ma. They suggest that this uplift could account for a component of Late Miocene uplift of the Altiplano region. Positive dynamic topography is also predicted for the eastern half of South America during Cenozoic times. A significant limitation of the dynamic topographic model proposed by *Flament et al*. [2015] and other predictive studies is the specific exclusion of contributions to surface dynamic topography made by buoyancy variations at depths shallower than ∼350 km. Consequently, these predictive models do not have short (∼1000 km) wavelength dynamic components.

Considerable attention has been paid to the effects of slab flattening [*Dávila et al*., 2010; *Eakin et al*., 2014; *Dávila and Lithgow-Bertelloni*, 2015]. For example, *Dávila and Lithgow-Bertelloni*[2013] suggest that the spatial pattern of dynamic topography along the Andean foreland is caused by changes in slab geometry between Early Miocene times and the present-day. In this model, continental-scale dynamic subsidence occurred in Early Miocene times along the foreland region, decreasing in amplitude above flat-slab segments that developed after the subduction of the Nazca, Juan Fernández, and Chile ridges. Regional uplift of southern Patagonia does not occur in their model because the effects of active upwellings are not considered. *Guillaume et al*. [2009] and *Guillaume et al*. [2013] simulate the evolution of southern Patagonia by allowing for opening of a slab window at the Chile ridge. *Guillaume et al*. [2009] model the spatiotemporal variation of dynamic uplift as the Chile triple junction migrates northward. They suggest that dynamic uplift of >800 m occurred up to 700 km away from the trench after 14 Ma. We predict that regional uplift of 1800 m commences at ∼20 Ma (Figure 10). Despite this apparent agreement, our results generally suggest that the present-day dynamic topography of South America is maintained at shorter wavelengths.

7 Conclusions

Quantitative modeling of drainage may prove to be a helpful tool for identifying and testing spatial and temporal patterns of regional uplift. Here, an inventory consisting of 1827 river profiles has been inverted to calculate a continent-wide uplift rate history for South America. River profiles were extracted from the SRTM database and modeled using a simplified version of

the stream-power formulation. The inverse problem was solved by seeking the smoothest uplift rate history through space and time that minimizes the misfit between observed and calculated river profiles based on a nonnegative least squares approach. Optimal erosional parameters were determined by inverting the drainage inventory and by honoring an independently determined uplift history for the Borborema Province of northeast Brazil. It is less straightforward to use inverse modeling of drainage networks to estimate regional subsidence.

Our calculated uplift rate history implies that a substantial proportion of the present-day topography grew during Cenozoic times. The Andean chain principally formed in Neogene times. These results are in general agreement with many geologic observations [*Isaks*, 1988; *Allmendinger et al.*, 1997; *Gregory-Wodzicki*, 2000; *Ramos and Ghiglione*, 2008; *Ramos*, 2009]. The precise timing of uplift of some areas, such as the Central Andean Altiplano, is still debated [*Barnes and Ehlers*, 2009]. Here, we provide an independent uplift rate history for the Altiplano that can be tuned to, and compared with, spot measurements. The smooth results suggest that slow uplift occurred in Oligocene times, followed by later discrete uplift events. The sedimentary flux history for the Foz do Amazonas suggests that increased deposition has occurred in response to regional uplift of the Northern and Central Andes since Mid-Miocene times.

Youthful regional uplift is also predicted for cratonic areas that are often considered to be old and stable. Geomorphologic and thermochronologic studies suggest that at least some of these regions underwent recent uplift [*Almeida et al.*, 2000; *Japsen et al.*, 2012; *Jelinek et al.*, 2014]. Remnants of extensive Cenozoic erosional surfaces occur in regions such as the Borborema Province, the Atlantic Shield, and the Guyanan Massif [*Freitas*, 1951; *McConnell*, 1968; *Briceño and Schubert*, 1990; *Peulvast et al.*, 2008]. These stepped surfaces appear to have ages that increase as a function of elevation, suggestive of regional episodic uplift. A range of observations imply that both the Borborema Province and the Altiplano of the Central Andes are at least partly generated and maintained by sub-plate processes. Many, but not all, models that calculate dynamic topography cannot resolve these shorter wavelength features. We suggest that inverse modeling of drainage networks might help to illuminate the way in which landscapes are sculpted by these sub-plate processes.

Acknowledgments